# The Extended COTS LPI Communication System

## Phase 3: Performance Analysis

J. C. Allen
M. Reuter
G. M. Dillard
G. Johnson
J. Zeidler

SSC San Diego

20001030 138

SPAWAR
Systems Center
San Diego

# The Extended COTS LPI Communication System

## Phase 3: Performance Analysis

J. C. Allen
M. Reuter
G. M. Dillard
G. Johnson
J. Zeidler

*SPAWAR*
*Systems Center*
*San Diego*

SSC San Diego
San Diego, CA 92152-5001

DTIC QUALITY INSPECTED 4

## ADMINISTRATIVE INFORMATION

SB

# Abstract

Phase 3 of the COTS LPI effort examines two LPI systems: LPI-1 approximates an incoherent M-ary orthogonal system; LPI-2, developed by Johnson [19], is a variant of the cyclic code-shift keying (CCSK) waveform. Each LPI system is assessed using the performance vector $[P_e \ E_b/N_0 \ R/W \ \text{SNR}]^T$. The SNR is included with the three standard COMM variables as a measure of covertness. Slices of this function are used to rank LPI-1 and LPI-2. For additive white Gaussian noise, the fundamental trade-off that emerges for fixed bandwidth $W$ is between the SNR and the bit rate $R$. A more covert system requires longer symbol vectors. These longer symbol vectors lower the bit rate. The LPI performance surface permits system engineers to graphically assess the trade-offs. For the multipaths of the Extended Littoral Battlefield, simulations show that multipath may either have no effect, improve performance, or, degrade performance. The basic observation is the longer symbol vectors can mitigate the multipath effects. Analysis of this multipath effect, increasing the bit rate, and migrating these results to an LPI performance surface are the basic Phase 4 recommendations.

# Contents

# 1

# The COTS LPI Communication Systems

## 1.1 Migrating COTS to LPI

The goal of this project is to migrate commercial off-the-shelf (COTS) technologies into military low-probability of intercept (LPI) applications. This task was undertaken by SPAWAR Systems Center, San Diego because commercial wireless companies cannot profitably invest research and development dollars for this military market. Phase 1 of this effort started by evaluating COTS cellular and COTS Wireless Local Area Networks for the Marine Corps Littoral Warfare Applications [14]. This evaluation showed that several COTS systems can be effective in many military applications with only minor modifications. However, these systems did not provide LPI communications for some littoral operations.

Phase 2 showed how to overcome these limitations [19]: "components developed for use by the COTS PCS systems could be used in a communications applique to provide LPI capability far beyond that of the original COTS system." The successful construction and deployment of a prototype LPI system demanded that this LPI capability be exploited.

Phase 3 undertakes this task to (1) model the LPI receiver, (2) analyze the basic LPI system performance, (3) assess LPI system performance in credible radio-frequency (RF) environments. This report documents this Phase 3 effort and lays the foundation for the Phase 4 effort.

Section 2 sets up a framework to analyze the LPI systems at baseband. Although the LPI waveform is not new, its implementation is novel and several LPI variants readily drop out of this framework. We analyze two LPI systems that delineate performance extrema: LPI-1 is an approximation to an M-ary orthogonal system, LPI-2 is a variation of cyclic code-shift keying (CCSK). Basic to any communication system is its probability of error. This section obtains the probability of symbol error

1

$P_e$ in additive white Gaussian noise (AWGN) and makes selected trade-offs with $E_b/N_0$ and the spectral efficiency $R/W$ [34]. However, the need for covertness places additional constraints on the system. A well-known and fundamental variable for covert RF operations is the signal-to-noise ratio (SNR). When trades-offs are made between the probability of error $P_e$, the spectral efficiency $R/W$, and the SNR, what emerges is a two-dimensional surface in $P_e \times R/W \times$ SNR space. We expect that RF mission planners will exploit this novel *LPI performance surface.*

Communication systems do not operate in white noise but must successfully overcome their RF environments. For example, anecdotes from the Persian Gulf describe how communication platforms could be seen but RF contact could not be made. Some LPI operations are the high-risk, covert forward deployments. It is unconscionable to put our forces in such high-risk deployments without proper RF mission planning. More generally, we cannot simply build an LPI system and hand it off without wrapping the system in an operational context. The trade-offs of bit rate, error, and covertness in the presence of multipath are non-trivial. For this reason, Section 3 analyzes the Extended Littoral Battlefield (ELB). The short-term objective is to have a suite of credible multipath scenarios to assess the LPI systems. The long-term objective is to understand RF propagation effects in the ELB and then bring this knowledge into RF mission planning and LPI deployments.

Section 4 uses the preceding results to assess LPI performance in the ELB multipath. ELB multipath can either degrade or improve LPI performance. For example, selecting the longer partial sequences for LPI-2 permitted it to overcome the multipath degradations in the HMMWV scenario. In fact, the longer sequences eventually permitted LPI-2 to beat the AWGN performance. In contrast, it was the shorter partial sequences for LPI-2 that gave better than AWGN performance in the Harbor scenario. Thus, the AWGN analysis and the ELB analysis provide benchmarks for assessing the LPI multipath performance. This stopping point is the natural starting point for Phase 4. Specifically, Phase 4 should undertake the following: (1) extend the analysis to additional LPI systems, (2) search for the presence of a noise floor, (3) increase the bit rate, (4) extend the ELB analysis to encompass the RF environmental effects, (5) assess the LPI performance in multipath, (6) develop these results into credible RF mission-planning tools.

## 1.2 Notation

The notation was selected to be consistent with as much of the literature as possible and to permit the reader to "drop in" on an equation without a lot of notational baggage. We follow Staley's notation in his excellent thesis [38] wherein the subscripts "$T$" and "$R$" denote the transmitter and receiver. Table 1.1 was designed with these rules and with an effort to reduce notational collisions.

Table 1.1: Notation.

| Symbol | Description |
|--------|-------------|
| $f$ | frequency (Hertz) |
| $f_c$ | carrier frequency (Hertz) |
| $f_e$ | fade rate (Hertz) |
| $f_D$ | maximal Doppler shift (Hertz) |
| $\Delta f_D$ | relative Doppler shift (Hertz) |
| $G_T$ | gain of transmitter's antenna |
| $G_R$ | gain of receiver's antenna |
| $G_0$ | free-space propagation gain |
| $h_T$ | transmitter's antenna height (feet) |
| $h_R$ | receiver's antenna height (feet) |
| $h(t,\tau)$ | Input Delay-Spread function |
| $h_{\mathrm{RF}}(t,\tau)$ | RF Input Delay-Spread function |
| $h_B(m,k)$ | Baseband Digital Input Delay-Spread function |
| $O_s$ | oversampling factor |
| $\lambda$ | wave length (meters) |
| $p_f(f)$ | Doppler scattering function |
| $p_\tau(\tau)$ | power delay profile |
| $p_T(t)$ | transmitter's pulse-shaping filter |
| $p_R(t)$ | receiver's matching filter |
| $P_T$ | power transmitted (Watts) |
| $P_R$ | power received (Watts) |
| $P_0$ | power in free-space (Watts) |
| $P_{xx}(f)$ | power spectrum of $\{x(t)\}$ |
| $R_{xx}(t_1,t_2)$ | covariance of $\{x(t)\}$ |
| $R$ | information bit rate (bits/sec) |
| $t$ | time (seconds) |
| $T$ | symbol duration (seconds) |
| $T_c$ | chip duration (seconds) |
| $\tau$ | delay (seconds) |
| $\Delta\tau$ | relative delay (seconds) |
| $\theta_g$ | grazing angle (radians) |
| $S_{xx}(f_1,f_2)$ | two-dimensional spectrum of $\{x(t)\}$ |
| $U(f,\tau)$ | Doppler-Delay function |
| $W$ | 3-dB bandwidth (Hertz) |
| $x_{\mathrm{RC}}(t)$ | raised cosine filter |

The Fourier transform of a signal $s(t)$ is

$$\widehat{s}(f) = \int_{-\infty}^{\infty} e^{-j2\pi ft} s(t)\,dt.$$

The convolution of $s(t)$ with a filter $h(t)$ is

$$h * s(t) = \int_{-\infty}^{\infty} h(t-\tau)s(\tau)\,d\tau.$$

A random process is denoted by $\{x(t)\}$. The covariance of $\{x(t)\}$ is

$$R_{xx}(t_1,t_2) = E[x(t_1)\overline{x(t_2)}],$$

where the complex conjugate is denoted by the overline. If $\{x(t)\}$ is harmonizable, then it admits a representation by a stochastic Fourier measure:

$$x(t) = \int_{-\infty}^{\infty} e^{+j2\pi ft}\,dX(f).$$

Equivalently, $R_{xx}(t_1, t_2)$ admits a representation as the two-dimensional Fourier transform of the covariance of $X(f)$:

$$R_{xx}(t_1, t_2) = \int_{-\infty}^{\infty} \int_{-\infty}^{\infty} e^{+j2\pi\{f_1 t_1 - f_2 t_2\}} dS_{xx}(f_1, f_2),$$

where $S_{xx}(f_1, f_2) = E[X(f_1)\overline{X(f_2)}]$. If $\{x(t)\}$ is *wide-sense stationary* (WSS), then it is standard to write $R_{xx}(t_1, t_2) = R_{xx}(t_1 - t_2)$. This is equivalent that the two-dimensional spectrum is supported on the main diagonal in the frequency plane: $S_{xx} = P_{xx}(f_1)\,\delta(f_1 - f_2)$, where $P_{xx}(f)$ is the usual power spectrum.

Matrix and vector notation is standard. A vector $\mathbf{x}$ is in column form with its size denoted $\mathbf{x} \sim N_{\mathbf{x}} \times 1$, where $N_{\mathbf{x}}$ denotes the number of rows of $\mathbf{x}$. Matrices are upper case $A$ with dimensions indicated as $A \sim M \times N$. The matrix transpose is $A^T$ and the conjugate transpose is $A^H$. The ubiquitous MATLAB grammar is also used. $A(:, n)$ denotes the $n$th column of matrix $A$. $A(m, :)$ denotes the $m$th row. The index vector is denoted $[1 : N] = [1\ 2\ \ldots N]$. Then $\mathbf{x}(3 + [1 : N]) = [x(3)\ x(4)\ldots x(N + 3)]^T$. The "floor" function rounds a real number toward $-\infty$: The "argmax" function is the inverse of the max function. If $h : \Omega \to \mathbf{R}$ and $h_{\max} = \max\{h(\omega) : \omega \in \Omega\}$ then $\operatorname{argmax}[h] := \{\omega \in \Omega : h(\omega) = h_{\max}\}$.

## 1.3   The Baseband System

Johnson's actual LPI system employs several non-trivial techniques to hide the features of the radiated power [19]. His system cleverly compensates for these parameter variations. By assuming optimal receiver operations, we ignore these variations and work from a fixed configuration. Thus, we estimate LPI performance for the generic baseband transmitter and receiver shown in Figure 1.1. The baseband assumptions (B-1, B-2, ... B-5) associated with this figure are listed next:
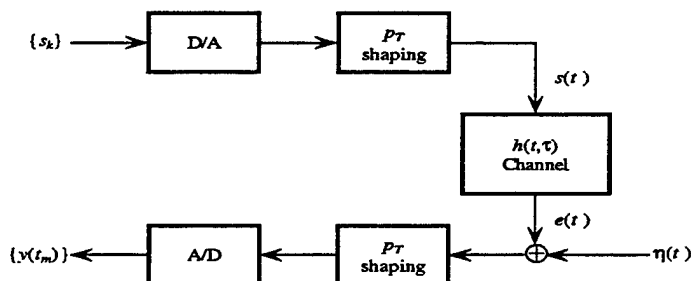


Figure 1.1: Baseband transmitter and receiver model

4

**B-1 Linear Modulation.** The signal $s_{RF}(t)$ transmitted at RF is obtained from the baseband signal $s(t)$ as

$$s_{RF}(t) = e^{+j2\pi f_c t}s(t).$$

**B-2 Linear Demodulation.** The received baseband signal $e(t)$ is demodulated from the RF signal as

$$e(t) = e^{-j2\pi f'_c t}\int_{-\infty}^{\infty} h_{RF}(t,\tau)s_{RF}(t-\tau)d\tau,$$

where $h_{RF}(t,\tau)$ denotes the RF Input Delay-Spread function.

**B-3 Perfect Synchronization.** The receiver and transmitter operate from a master clock.

**B-4 Matched Filter.** The convolution of the transmitter filter $p_T(t)$ and the receiver filter $p_R(t)$ is the raised cosine filter [34, pages 63–65]: $p_R * p_T(t) = x_{RC}(t)$.

**B-5 Slow Fading.** The Baseband Input Delay-Spread function has the form:

$$h(t,\tau) = \sum_{n=1}^{N} a_n(t)\delta(\tau - \tau_n),$$

where the $\{a_n(t)\}$'s are JWSS complex Gaussian with mean and spectral shape determined by the propagation environment and the RF modulations. The "slow-fading" assumption is that the maximal spectral extent of the $\{a_n(t)\}$'s is "small" with respect to the bandwidth of the receiver filter $p_R(t)$.

Following [30] and [18], the baseband channel input has the complex baseband form:

$$s(t) = \sum_{k=-\infty}^{\infty} s_k p_T(t - kT_c),$$

where the $s_k$'s will be the "chips" ($s_k = \pm 1$) from various PN sequences. The baseband receiver output is modeled as

$$y(t) = p_R * e(t) + p_R * \eta(t),$$

where $\{\eta(t)\}$ is a complex-valued, zero-mean, white Gaussian random process with two-sided power spectral density $2N_0$. The slow fading assumption permits the approximation [1, Eq. 3.2]:

$$y(t) \approx \sum_{k=-\infty}^{\infty} \sum_{n=1}^{N} s_k a_n(t)x_{RC}(t - \tau_n - kT_c) \; + \; p_R * \eta(t). \tag{1.1}$$

5

For the additive white-noise Gaussian channel, $h(t, \tau) = a\delta(t)$. In this case, the receiver's output is

$$y(t) \approx a \sum_{k=-\infty}^{\infty} s_k x_{\mathrm{RC}}(t - kT_c) + p_R * \eta(t).$$

By B-3, ideal symbol timing is possible. That is, the receiver may sample $y(t)$ at instants $t_m = mT/O_s$, where $O_s$ denotes the oversampling factor. With $O_s = 1$, digital input to the demodulator has no ISI and then has the form:

$$y(t_m) = s_m + g_m, \tag{1.2}$$

where $\{g_m\}$ is Gaussian IID.

# 2

# LPI Performance in AWGN

This section establishes a baseline performance of the LPI systems. A generic base-band transmitter and receiver are assumed (Section 1.3). The channel is additive white Gaussian noise (AWGN). For each noise level and each receiver parameter, we obtain an LPI performance vector $[P_e \; E_b/N_0 \; R/W \; \text{SNR}]^T$. The SNR is used as a simple measure of covertness. As we sweep over the noise levels and detector parameters, the resulting performance vectors generate an LPI performance manifold. Slices of this manifold provide handy graphics of the LPI performance. For example, we will see that each LPI system determines a two-dimensional manifold in $P_e \times R/W \times \text{SNR}$ space. If a system engineer or RF mission planner needs an operational SNR and probability of symbol error, then the spectral efficiency is not also independent but located on the manifold at a point determined by the SNR and $P_e$. With the spectral efficiency then fixed, a bit-rate requirement will set the actual bandwidth. That is, the LPI geometry determines RF and receiver parameters. Thus, a useful LPI mission tool is developed for each of the LPI receivers. A glance at the table of contents will show that for each LPI system, we estimate the theoretical performance, examine the LPI settings in noise, and collect all these results in the final system performance (the LPI manifold).

## 2.1  Parameterizing the LPI Systems: $[N_p, N_\Delta, N_u]$

The generic LPI scheme is a variant of non-coherent M-ary orthogonal signaling using symbol vectors $\mathbf{u}_1$, $\mathbf{u}_2$, ..., $\mathbf{u}_L$. The $\mathbf{u}_l$'s are obtained from a *generalized partition* of a PN sequence $\mathbf{u}$ consisting of $\pm 1$'s of length $N_u$. Currently, the $\mathbf{u}_l$'s all have the same length $N_p$. $N_p$ is also called the partial length and $1 \ll N_p \le N_u$. The indices of adjacent symbol vectors may overlap by length $0 \le N_\Delta < N_p$. For $l = 1, \ldots, L$

$$\mathbf{u}_l = \mathbf{u}(\; (l-1) \times (N_p - N_\Delta) + [1 : N_p] \;),$$

7

where cyclic wrapping of $\mathbf{u}$ is assumed when necessary. Although the symbol vectors are not orthogonal, the goal is to have small cross correlations. This tends to be true for large $N_p$ and $N_u$ because of the "white noise" nature of the PN sequences. Thus, the variables $(N_p, N_\Delta, N_u)$ can be viewed as three "knobs" that dial in the desired performance from the corresponding LPI receiver.

This report typically fixes at $N_u = 2^{16}$ but varies the partial length $N_p$ and overlap $N_\Delta$. LPI-1 takes the overlap to be $N_\Delta = 0$ so that the symbol vectors are a partition of the PN sequence $\mathbf{u}$. In contrast, LPI-2 uses maximal overlap $N_\Delta = N_p - 1$ so that many more symbol vectors are available in comparison to LPI-1. We will see that this gives LPI-2 a higher spectral efficiency but at the expense of covertness and sensitivity to multipath.

## 2.2   LPI-1: An M-ary LPI Scheme with $N_\Delta = 0$

LPI-1 is a variant of non-coherent M-ary orthogonal signaling using symbol vectors $\mathbf{u}_1, \mathbf{u}_2, \ldots, \mathbf{u}_L$. The $\mathbf{u}_l$'s are obtained from a partition of a PN sequence $\mathbf{u}$. Consequently, the symbol vectors are not orthogonal but have small cross correlation. The baseband assumptions, with B-3 modified to include the knowledge of these symbol vectors and their transmission times, give the vector form of the detector's input (See Equation 1.2):

$$\mathbf{y} = [y(t_m)] = a\mathbf{u}_l + \mathbf{g}.$$

For the simulations, we take $\mathbf{u}_l$'s to be non-overlapping with length $N_p$. If the entire PN sequence has length $N_u$ then there are

$$L = \text{floor}(N_u/N_p)$$

symbol vectors. This $L$ will be used throughout the LPI-1 analysis. If $N_p L < N_u$ then the trailing chips are dropped. Form the matrix

$$U = [\mathbf{u}_1 \ \mathbf{u}_2 \ \ldots \mathbf{u}_L] \sim N_p \times L.$$

The detector output may be written as

$$\widehat{l} = \text{argmax}(|U^H \mathbf{y}|).$$

### 2.2.1   $P_e$ Estimates

Because the detector uses magnitude only, the channel loss may be scaled into the noise. Let $\widetilde{\mathbf{y}}$ denote this scaled input vector to the detector. Then

$$\widetilde{\mathbf{y}} = \mathbf{u}_l + \mathbf{g},$$

where $\mathbf{g} \sim \mathcal{N}(0, \sigma_g^2 I)$. The SNR at the detector's input is the ratio of mean energy in the symbol vector to the noise energy:

$$\text{SNR} = \frac{1}{\sigma_g^2}.$$

We estimate the probability of error as a function of this SNR. Let $\mathbf{r}$ denote a scaled version of the detected vector:

$$\mathbf{r} = \frac{1}{N_p} U^H \tilde{\mathbf{y}} = \frac{1}{N_p} U^H \mathbf{u}_l + \frac{1}{N_p} U^H \mathbf{g}.$$

Following Miller [27, page 77], the probability density of $\mathbf{r}$ given $l$ is

$$p(\mathbf{r}|l) = \frac{1}{\pi^{N_p} \det[R]} \exp\left(-(\mathbf{r} - \mathbf{r}_l)^H R^{-1} (\mathbf{r} - \mathbf{r}_l)\right),$$

where

$$\mathbf{r}_l = \frac{1}{N_p} U^H \mathbf{u}_l \quad \text{and} \quad R = \frac{\sigma_g^2}{N_p^2} U^H U.$$

Assuming all $L$ symbols equally likely gives the probability of symbol error as

$$P_e = \sum_{l=1}^{L} P[\hat{l} \neq l | l]\, P[l] = \frac{1}{L} \sum_{l=1}^{L} P[\hat{l} \neq l | l].$$

The problem is to estimate $P[\hat{l} \neq l | l]$ to determine the symbol error $P_e$.

*An Orthogonal Approximation:* Because $U \sim N_p \times L$ is formed from a PN sequence, it is approximately orthogonal: $U^H U \approx N_p \times I_L$. Then, assuming $\mathbf{r}_l$ was transmitted, $\mathbf{r}$ admits the approximate distribution:

$$\mathbf{r} \approx \begin{cases} 1 + \mathcal{N}(0, \sigma_g^2 / N_p) & l' = l \\ \mathcal{N}(0, \sigma_g^2 / N_p) & l' \neq l \end{cases}.$$

That is, the components of $\mathbf{r}$ are approximately independent and complex Gaussian. Then the components of $|\mathbf{r}|$ are approximately independent and Ricean [34, page 47]:

$$p_{l'|l}(r) \approx 1_{[0,\infty)}(r) \frac{r}{\sigma^2} \begin{cases} e^{-(r^2+1)/2\sigma^2} I_0(r/\sigma^2) & l' = l \\ e^{-r^2/2\sigma^2} & l' \neq l \end{cases},$$

where $\sigma^2 = \sigma_g^2 / (2N_p)$. Then the joint probability density of $|\mathbf{r}|$ is

$$p_{1,2,\dots,L|l}(r_1, r_2, \dots, r_L) \approx p_{1|l}(r_1) p_{2|l}(r_2) \dots p_{L|l}(r_L).$$

Then the probability of a correct decision $P[\hat{l} = l | l]$ is the integral of the joint density over the set

$$\mathcal{R}(l) = \{\mathbf{r} \in \mathbf{R}^L : r_l > r_{l'} \text{ for } l' = 1, \dots L, l' \neq l\}.$$

9

More formally [37, page 179],

$$
\begin{aligned}
P[\widehat{l} = l | l] &= \mathrm{Prob}[|\mathbf{r}(l)| \geq |\mathbf{r}(l')| \ \text{for } l' = 1, \ldots, L, l' \neq l] \\
&= \int_{\mathcal{R}(l)} p_{1,2,\ldots,L|l}(r_1, r_2, \ldots, r_L) \, dr_1 dr_2 \ldots dr_L \\
&\approx \int_0^\infty dr_l \, p_{l|l}(r_l) \prod_{\substack{l' \neq l \\ l'=1}}^{L} \int_0^r dr_{l'} \, p_{l'|l}(r_l') \\
&= \int_0^\infty \frac{r}{\sigma^2} e^{-(r^2+1)/2\sigma^2} \, I_0(r/\sigma^2) \{1 - e^{-r^2/2\sigma^2}\}^{L-1} dr \\
&= \sum_{l'=0}^{L-1} \frac{(-1)^{l'}}{l'+1} \binom{L-1}{l'} e^{-l'/2\sigma^2(l'+1)}.
\end{aligned}
$$

This result shows that the probability of a correct decision is, with respect to this approximation, not dependent on $l$. Then, for any $l$ there holds

$$
P_e = \frac{1}{L} \sum_{l'=1}^{L} P[\widehat{l} \neq l | l] = P[\widehat{l} \neq l | l] = 1 - P[\widehat{l} = l | l].
$$

The following simulations demonstrate the quality of this approximation using symbol vectors on the order of Johnson's systems.

## 2.2.2 $P_e$ for $[N_p, N_\Delta, N_u] = [1024, 0, 2048]$

A low-dimensional simulation illustrates this PPM system. The PN sequence[1] **u** has length $N_u$=2048. With partial length $N_p = 1024$, the correlator is nearly orthogonal:

$$\frac{1}{N_p}U^H U = \begin{bmatrix} 1.0000 & -0.0215 \\ -0.0215 & 1.0000 \end{bmatrix}.$$

Figure 2.1 compares the simulation with the $P_e$ estimate. An excellent fit is obtained provided we observe that the number of simulations (100,000) limit the trustworthy estimates to $P_e > 10^{-4}$. A rule-of-thumb is that $U$ becomes "orthogonal" provided $N_p > N_u/10$ [1]. For system applications, increasing $N_p$ permits a lower SNR but reduces the bit rate. These trade-offs are explored next.
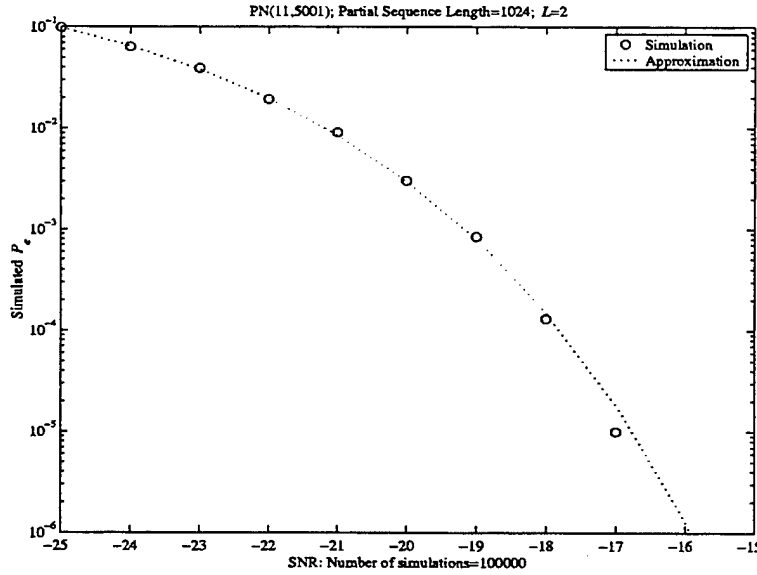


Figure 2.1: Comparison of $P_e$ (symbol error) simulations and approximation for $[N_p, N_\Delta, N_u] = [1024, 0, 2048]$.

---

[1]Generated as **u** = pn_scr$(11, 5001, N_u, 1)$ from [31]

11

## 2.2.3 $P_e$ for $[N_p, N_\Delta, N_u] = [1024, 0, 2^{16}]$

A simulation more in line with one of Johnson's LPI systems uses a PN sequence[2] **u** of length $N_u = 2^{16}$. With partial length $N_p = 1024$, we are well below the 10% rule. Consequently, the approximation is more crude with

$$\frac{1}{N_p} U^H U = I + E,$$

where most of the elements of $E$ are still small (mean magnitude $\approx 0.02$). However, a few elements have magnitude $\approx 0.1$. Although the orthogonal approximation is degraded, it still gives good $P_e$ estimates as shown in Figure 2.2. Although LPI-1 with $L = 64$ has 6 times the bit rate as the system with $L = 2$, the SNR must increase for comparable symbol error rates, as can be seen by comparing Figures 2.1 and 2.2.
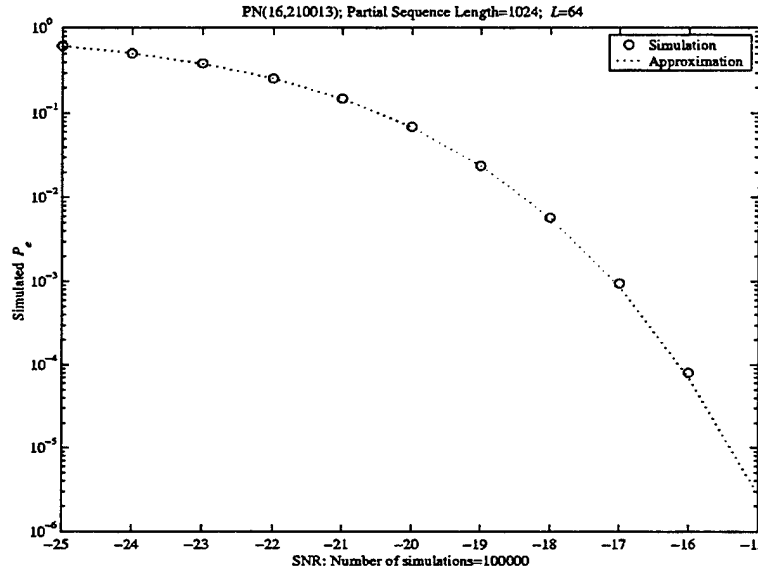


Figure 2.2: Comparison of $P_e$ (symbol error) simulations and the approximation for $[N_p, N_\Delta, N_u] = [1024, 0, 2^{16}]$.

---

[2]Generated as **u** = pn_scr$(16, 210013, N_u, 1)$ from [31].

## 2.2.4 System Performance: $[N_p, N_\Delta, N_u] = [N_p, 0, 2^{16}]$

This section presents performance trade-offs for the LPI-1 system. We start by comparing several partial lengths $N_p$ in Figure 2.3. The longer partial lengths permit operation in lower SNR but reduce the information bit rate $R$.
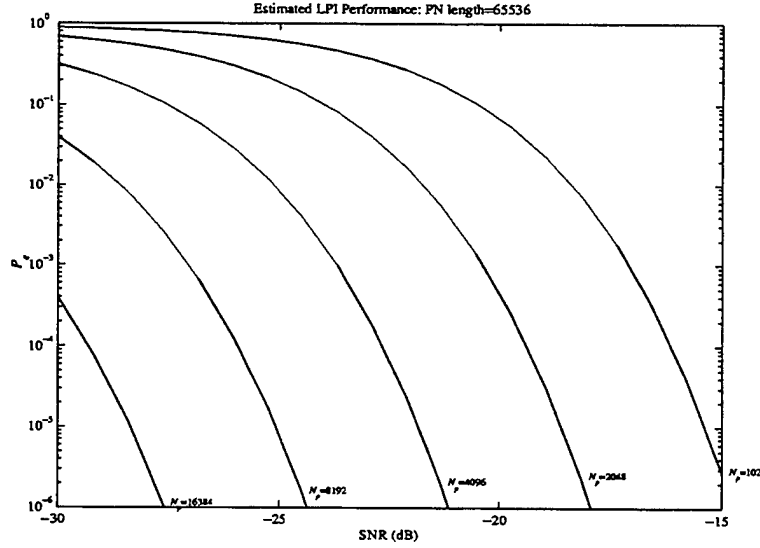


Figure 2.3: Comparison of $P_e$ (approximations) against SNR for partial lengths $N_p$ for $[N_\Delta, N_u] = [0, 2^{16}]$.

To quantify this statement, let each chip have duration $T_c$. With the raised-cosine pulse, the 3-dB bandwidth is $W = 1/T_c$. Each symbol vector has duration $T = N_p T_c$ so that the information bit rate is

$$R = \frac{\log_2(L)}{N_p T_c} \quad \text{[bits/sec]}.$$

The spectral efficiency is [34, pages 282-284]

$$\frac{R}{W} = \frac{\log_2(L)}{N_p} \quad \text{[bits/sec/Hz]}.$$

Figure 2.4 plots the resulting LPI performance curves as a function of the partial lengths $N_p$ This plot is really a "skeleton" of the LPI performance surface. That is, LPI performance variables SNR, $P_e$, $R/W$ are constrained to lie a surface. For clarity, we only plot the associated lines. This surface reveals the LPI the trade-offs: more covertness or low SNR requires longer partial lengths that reduce $R$. This surface is also assists RF mission planning. For example, a glance at Figure 2.4 shows that $R/W$ is a function of SNR and $P_e$. If the covertness requirements set the SNR near

13

-25 dB and the error requirements are $10^{-4}$ then $R/W \approx 0.1$ bits/sec/Hz. To get 2400 bits per second dictates a bandwidth of approximately 24 kHz. This surface also shows the RF mission planner what trade-offs can be made if the desired operational point is not feasible. For example, if $R/W$ must be near 1 bits/sec/Hz then we can either (1) relax $P_e$ to $10^{-2}$, (2) relax SNR to -20 dB, (3) or simultaneously relax $P_e$ to $10^{-3}$ and the SNR to -23 dB.
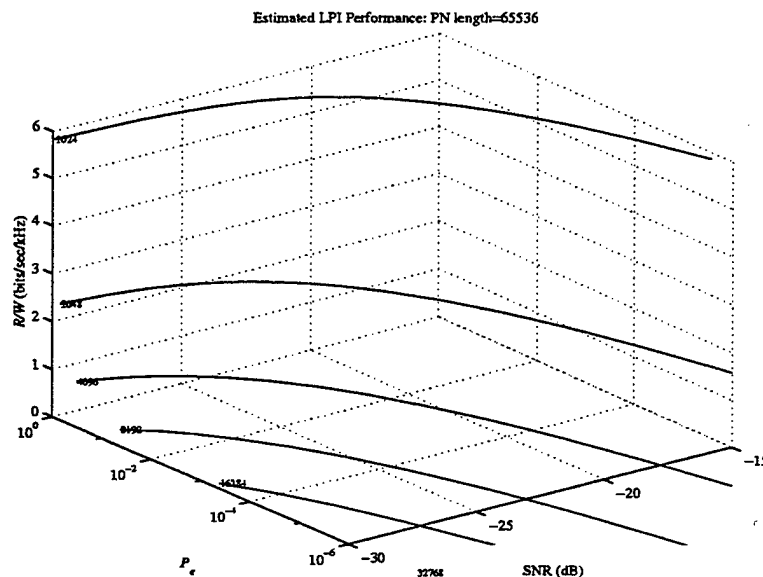


Figure 2.4: LPI performance as function of partial lengths $N_p$ for $[N_\Delta, N_u] = [0, 2^{16}]$.

We close with the standard $E_b/N_0$ plots. $E_b/N_0$ is derived from the SNR as

$$\frac{E_b}{N_0} = \frac{N_p}{\log_2(L)} \times \text{SNR}.$$

Figure 2.5 plots $P_e$ as a function of $E_b/N_0$. This figure agrees with Figure 3.34 in Sklar [37] for non-coherently detected M-ary orthogonal signaling, noting the bit error versus symbol error difference between the plots. This performance curve applies to all M-ary orthogonal signaling, regardless of spectral efficiency. Figure 2.6 plots spectral efficiency against $E_b/N_0$. Comparing Figure 2.6 with the bandwidth-efficiency plane in Figure 7.6 of [37], we see that LPI-1 performance exists in the swath of $E_b/N_0$ from 7 to 11 dB, which agrees with MFSK performance. However, the LPI nature of the waveform comes at the expense of spectral efficiency, which is much less than that of the corresponding MFSK waveforms. Also, all of the LPI-1 waveforms in Figure 2.5 and 2.6 have the same bandwidth, in contrast to MFSK in Figure 7.6 of [37]. So, as $L$ decreases in LPI-1, the spectral efficiency also decreases. These figures reveal a trade-off. Although the longer sequences are more covert in terms of the received SNR, the lower data rates associated with these sequences result in a loss in performance with respect to $E_b/N_0$ and spectral efficiency.
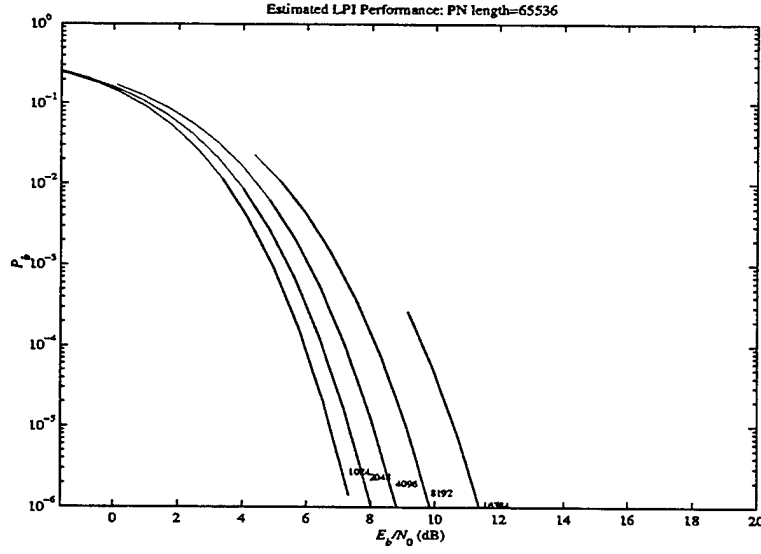
14

Figure 2.5: Comparison of $P_b$ (bit error) against $E_b/N_0$ for partial lengths $N_p$: $N_u = 2^{16}$. Each line from left to right is determined by the partial lengths $N_p$=1024, 2048, 4096, 8192, 16384.
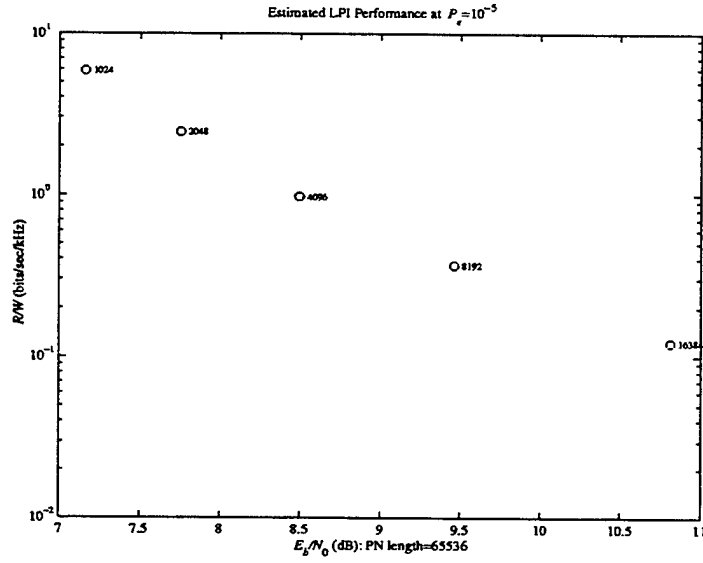


Figure 2.6: Comparison of $R/W$ against $E_b/N_0$ for partial lengths $N_p$ for $N_\Delta = 0$ and $N_u = 2^{16}$.

15

## 2.3    LPI-2: A CCSK LPI Scheme with $N_\Delta = N_p - 1$

Johnson invented an LPI system based on cyclic code-shift keying (CCSK) [19]. As before, we assume Johnson's receiver compensates for his LPI parameter variations. The CCSK scheme starts from a given PN sequence $\mathbf{u}$ of length $N_u$. The symbols $l = 0, 1, \ldots N_u - 1$ are mapped to cyclic shifts of $\mathbf{u}$. Thus, the $l$th symbol vector for CCSK is

$$\mathbf{u}_l = u(\text{rem}(l + [1 : N_u], N_u))$$

with $L = N_u$ symbol vectors.[3] To increase the bit rate, Johnson invented a partial CCSK system by exploiting the almost orthogonality of $\mathbf{u}$ by only transmitting the first $N_p$ chips of $\mathbf{u}_l$. That is, the $l$th symbol vector for partial CCSK is

$$\mathbf{u}_l = u(\text{rem}(l + [1 : N_p], N_u)).$$

These $L$ symbol vectors each carry $\log_2(N_u)$ bits of information. The baseband assumptions give that the vector form of the detector's input (See Equation 1.2):

$$\mathbf{y} = [y(t_m)] = a\mathbf{u}_l + \mathbf{g}.$$

The detector output is

$$\widehat{l} = \text{argmax}(|\mathbf{u} \star_c \mathbf{y}|),$$

where the subscript "c" denotes circular correlation.

### 2.3.1    $P_e$ Estimates

Because only the magnitude matters for the detector, we scale the channel loss into the noise. If $\widetilde{\mathbf{y}}$ denotes this scaled input vector to the detector then

$$\widetilde{\mathbf{y}} = \mathbf{u}_l + \mathbf{g},$$

where $\mathbf{g} \sim \mathcal{N}(0, \sigma_g^2 I)$. The SNR at the detector's input is the ratio of the mean energy in the symbol vector to the variance of the complex additive Gaussian noise:

$$\text{SNR} = \frac{1}{\sigma_g^2}.$$

We estimate the probability of error as a function of this SNR. Introduce the $N_u \times N_p$ circulant matrix $C_u$ to model the cyclic correlation with $\mathbf{u}$:

$$\mathbf{u} \star_c \mathbf{u}_l = C_u \mathbf{u}_l.$$

---

[3] "rem" denotes the remainder function. For brevity, indexing starts at 0.

Let $\mathbf{r}$ denote a scaled version of the detected vector:

$$\mathbf{r} = \frac{1}{N_p}C_u\tilde{\mathbf{y}} = \frac{1}{N_p}C_u\mathbf{u}_l + \frac{1}{N_p}C_u\mathbf{g}.$$

The scaling is rigged so that the maximum of the correlation is 1. Following Miller [27, page 77], the probability density of $\mathbf{r}$ given $l$ is

$$p(\mathbf{r}|l) = \frac{1}{\pi^{N_p}\det[R]}\exp\left(-(\mathbf{r}-\mathbf{r}_l)^H R^{-1}(\mathbf{r}-\mathbf{r}_l)\right),$$

where $\mathbf{r}_l = C_u\mathbf{u}_l/N_p$ and the noise has the covariance matrix

$$R = \frac{\sigma_g^2}{N_p^2}C_u C_u^H \approx \frac{\sigma_g^2}{N_p}I.$$

Then $\mathbf{r}$ is approximately distributed as

$$\mathbf{r} \approx \begin{cases} 1 + \mathcal{N}(0,\sigma_g^2/N_p) & l' = l \\ \mathcal{N}(0,\sigma_g^2/N_p) & l' \neq l \end{cases}.$$

That is, the components of $\mathbf{r}$ are approximately independent and complex Gaussian. This is the approximation used in Section 2.2.1. With each symbol equally likely,

$$P_e = \frac{1}{N_u}\sum_{l'=0}^{N_u-1}P[\hat{l}\neq l|l].$$

The probability of a correct decision is approximately

$$\begin{aligned} P[\hat{l} = l|l] &\approx \int_0^\infty \frac{r}{\sigma^2}e^{-(r^2+1)/2\sigma^2}I_0(r/\sigma^2)\{1-e^{-r^2/2\sigma^2}\}^{N_u-1}dr \\ &= \sum_{l'=0}^{N_u-1}\frac{(-1)^{l'}}{l'+1}\binom{N_u-1}{l'}e^{-l'/2\sigma^2(l'+1)}, \end{aligned}$$

where $\sigma^2 = \sigma_g^2/(2N_p)$. This shows the probability of a correct decision is, with respect to this approximation, not dependent on $l$. Then, for any $l$,

$$P_e = P[\hat{l}\neq l|l] = 1 - P[\hat{l} = l|l].$$

The quality of this approximation is assessed in the following subsections.

## 2.3.2 $P_e$ for $[N_p, N_\Delta, N_u] = [1024, 1023, 2^{16}]$

The PN sequence[4] $\mathbf{u}$ has length $N_u$=65,536. The partial lengths are set to $N_p$=1024 for comparison with the LPI-1 (M-ary) simulations. In the LPI-1 simulation of Section 2.2.3, each $N_p$=1024 chips carried 6 bits. In this LPI-2 simulation, each partial

---

[4]Generated by $\mathbf{u} = \text{pn\_scr}(16, 210013, N_u, 1)$ from [31].

sequence of $N_p=1024$ chips carries 16 bits of information. Consequently, the bit rate for LPI-2 has increased by a factor of $2.7=16/6$ over LPI-1. In comparison to standard CCSK, the bit rate for LPI-2 has increased by a factor of 64. However, increasing the bit rate incurs a loss of covertness. Figure 2.7 illustrates this point by comparing LPI-2 against LPI-1. Although the partial sequence length $N_p$ is the same for both LPI-1 and LPI-2, there are $2^{10}$ more symbol vectors in the LPI-2 symbol set. Therefore, more potential symbol errors are possible in LPI-2 versus LPI-1. As a result, LPI-2 requires a higher SNR for comparable $P_e$ performance.
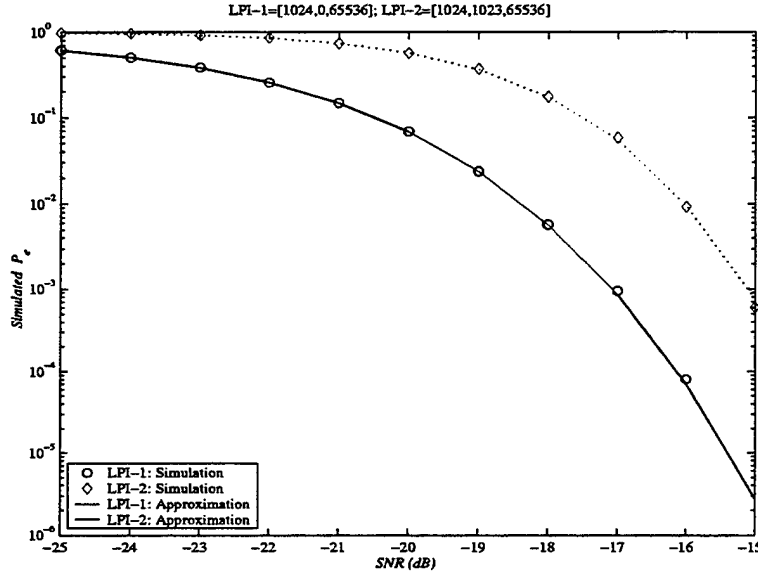


Figure 2.7: Comparing $P_e$ for LPI-1 (M-ary) $[N_p, N_\Delta, N_u] = [1024, 0, 2^{16}]$ against LPI-2 (partial CCSK) with $[N_p, N_\Delta, N_u] = [1024, 1023, 2^{16}]$.

## 2.3.3 $P_b$ for $[N_p, N_\Delta, N_u] = [2^{16}, 2^{16} - 1, 2^{16}]$

Although a special case of partial CCSK with $N_p = N_u$, Figure 2.8 compares the theoretical approximations with measurements obtained by George B. Johnson in November 1999. Agreement between theory and measurements demonstrate that reasonable modeling of the COTS LPI system has been obtained. Here the bit error $P_b$ is plotted and relates to the symbol error $P_e$ as [34, page 311]:

$$P_b = \frac{2^{M-1}}{2^M - 1} P_e,$$

where $M = \log_2(L)$ is the number of bits carried by each symbol vector. What is striking about this figure is the low SNR that may be obtained using the long PN sequences. This reduction in SNR costs in terms of the bit rate. Consequently, the next section completes this examination of CCSK by making the bit rate versus SNR trade-off.
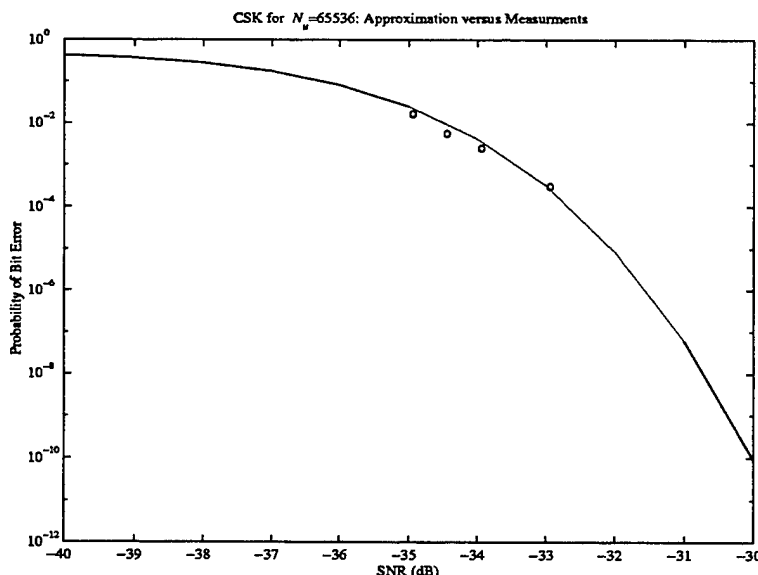
Figure 2.8: Comparing bit error estimates between the measurements and theory for standard CCSK: $[N_p, N_\Delta, N_u] = [2^{16}, 2^{16} - 1, 2^{16}]$.

## 2.3.4 System Performance: $[N_p, N_\Delta, N_u] = [N_p, N_p - 1, 2^{16}]$

This section offers performance trade-offs for the LPI-2 (partial CCSK) system. For a fixed PN length $N_u$=65536, we compare several partial lengths $N_p$ in Figure 2.9. The longer partial lengths permit operation in lower SNR, but reduce the information bit rate $R$. To quantify this statement, let each chip have duration $T_c$. With the raised-cosine pulse, the 3-dB bandwidth is $W = 1/T_c$. Then each symbol vector has duration $T = N_p T_c$. Recall that each symbol vector carries $\log_2(N_u)$=16 bits. The information bit rate is

$$R = \frac{\log_2(N_u)}{N_p T_c} \quad \text{[bits/sec]}.$$

The spectral efficiency is [34, pages 282-284]:

$$\frac{R}{W} = \frac{\log_2(N_u)}{N_p} \quad \text{[bits/sec/Hz]}.$$

Figure 2.10 plots the resulting LPI performance curves as a function of the partial lengths $N_p$. The more covert operation (SNR$\ll$1) requires longer partial lengths with the subsequent reduction of $R$. $E_b/N_0$ is given by

$$\frac{E_b}{N_0} = \frac{N_p}{\log_2(N_u)} \times \text{SNR}.$$

Figure 2.11 plots $P_e$ as a function of $E_b/N_0$. This plot reveals how misleading $E_b/N_0$ performance measures are for an LPI system. Although the longer sequences operate in lower SNR environments as Figure 2.9 shows, there is a decrease in the bit rate such that $E_b/N_0$ is identical for all these sequences. Figure 2.11 also does not have the familiar form of Figure 3.34 in [37] for non-coherently detected orthogonal signaling because each of the partial-length symbols LPI-2 encodes *the same number of bits*. Each curve in Figure 2.11 falls on the $M = 2^{16}$ curve in Figure 3.34 in [37], although the spectral efficiently differs for each waveform as Figure 2.10 shows.
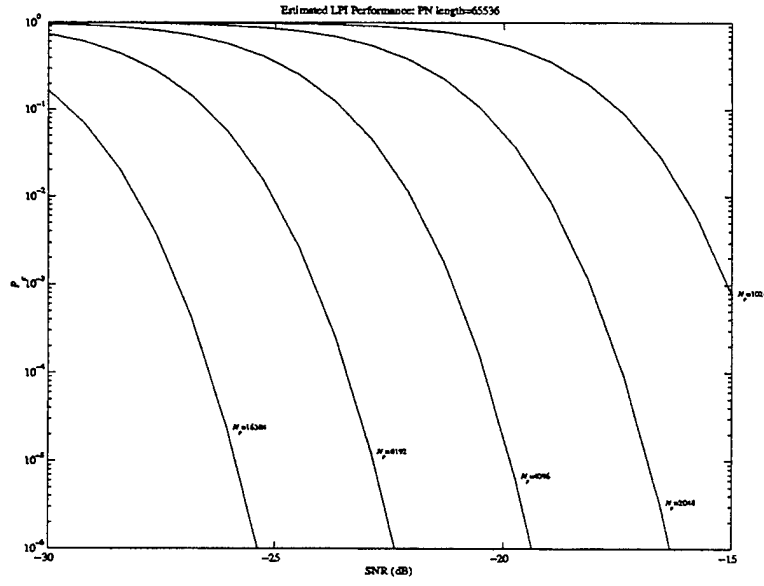
Figure 2.9: Comparison $P_e$ (symbol error) against SNR for partial lengths $N_p$: $[N_p, N_\Delta, N_u] = [N_p, N_p - 1, 2^{16}]$.
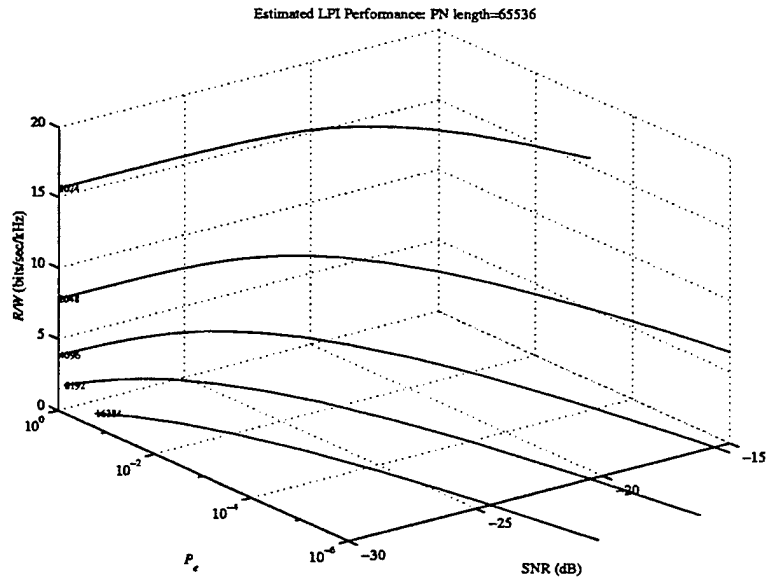


Figure 2.10: LPI-2 performance as function of partial lengths $N_p$: $[N_p, N_\Delta, N_u] = [N_p, N_p - 1, 2^{16}]$.
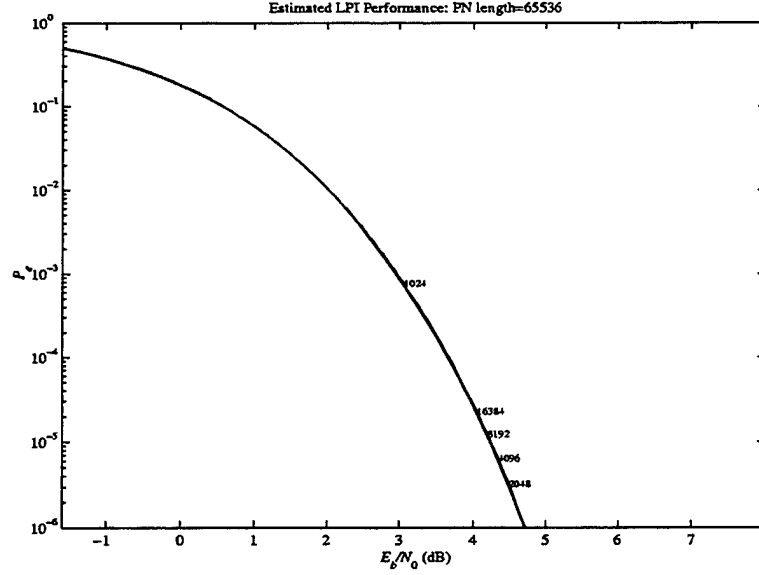
21

Figure 2.11: Comparison of $P_e$ (symbol error) against $E_b/N_0$ for partial lengths $N_p$: $[N_p, N_\Delta, N_u] = [N_p, N_p - 1, 2^{16}]$.

## 2.4   Parameterizing the LPI Performance

This section concludes by showing the conjectured mapping of the LPI parameters $[N_p, N_\Delta, N_u]$ to the system performance $[P_e, R/W, \text{SNR}]$ in additive white Gaussian noise with variance $\sigma_g^2$. The approximations are good for LPI-1 and LPI-2 over the $[N_p, N_\Delta, N_u]$ values used in this section. It remains to be seen how well the approximations hold over the entire three-parameter LPI family. Given $[N_p, N_\Delta, N_u]$ assume that $L$ symbol vectors $\mathbf{u}_1, \ldots, \mathbf{u}_L$ are transmitted. The computation of $L$ depends on the generalized partition and the cyclic wrapping of $\mathbf{u}$. If no cyclic wrapping is used then $L$ is bounded as

$$L \le \frac{N_u - N_\Delta}{N_p - N_\Delta}.$$

For LPI-1, there are $L = \text{floor}(N_u/N_p)$ symbol vectors. For the CCSK in LPI-2, cyclic wrapping gives $L = N_u$ symbol vectors.

The SNR is the ratio of the mean energy in the symbol vector to the variance of the complex additive Gaussian noise:

$$\text{SNR} = \frac{1}{\sigma_g^2}.$$

22

The spectral efficiency is the rato of the bit rate $R$ to the bandwidth $W$:

$$\frac{R}{W} = \frac{\log_2(L)}{N_p},$$

where each chip has duration $T_c$. For the probability of symbol error, the current conjecture is that

$$P_e \approx 1 - \sum_{l'=0}^{L-1} \frac{(-1)^{l'}}{l'+1} \binom{L-1}{l'} \exp\left(-\frac{N_p}{\sigma_g^2} \frac{l'}{l'+1}\right).$$

This approximation appears to be good for LPI-1 with $L = \text{floor}(N_u/N_p)$ and LPI-2 with $L = N_u$. Assessing the range of validity of these formulas is one the Phase 4 tasks mentioned in the beginning of this report. Likewise, extending these trade-off formulas to multipath environments is another Phase 4 task. Finally, a synthetic case of multipath is to overlap the symbol vectors in time. This increases the bit rate but should also increase the SNR and error rate. Quantifying the trade-off between bit rate and covertness is a Phase 4 task.

# 3

# The ELB Channel Models

Section 2 determined LPI performance in additive white Gaussian noise. For real-world operations, the LPI performance must be assessed in operationally credible multipath. Referring to the baseband system in Figure 1.1, this means that an Input Delay-Spread function $h(t, \tau)$ needs to be specified, in addition to the additive noise. Extended Littoral Battlefield (ELB) multipath provides an excellent "testbed" for such an assessment. This section presents three ELB channel models to be used in the multipath simulations of Section 4:

**Bluewater.** Mobile ship in bluewater to shore site.

**Harbor.** Mobile ship in urban harbor to shore site

**HMMWV.** Mobile HMMWV in urban environment to shore site.

These ELB channel models are derived from the *Naval Communication Channels (NCC) Dataset*. The NCC Dataset contains over-the-air measurements of a mobile HMMWV and a mobile Navy ship transmitting to a fixed shore site at 1 Mbps in the 225 to 400 MHz military UHF band collected at San Diego, California during January and February of 1998 [1]. As such, these experiments are representative of urban Marine Corps and the Naval communications in the ELB.

This section analyzes this ELB dataset. The immediate goal provides collection of credible ELB channel models for LPI multipath. The long-term goal develops an understanding of ELB propagation for RF mission planning and LPI deployments. Section 3.1 reviews general channel models. Section 3.2 specializes these models to the ELB propagation environment Section 3.3 describes the receiver and transmitter, the data acquisition process, the routes of the ship and HMMWV. Comparison with measurements indicate that a Ricean model provides an upper bound on the received power levels. Section 3.4 describes channel estimation from noisy, distorted, digitized versions of the RF signal that probed the ELB channels. The remaining sections each describe the bluewater, harbor, and HMMWV channel models. The goal is to reduce

each channel to a table listing each path, its power level, delay, Doppler, fade rate, and fading processes. These tables are the end product of this effort. The channel modeler can simply turn to these tables to program a channel emulator or continue to the next section that puts the LPI systems into these channels.

## 3.1   General Channel Models

Bello's seminal 1963 paper established the nomenclature and analysis for stochastic time-variant linear channels [5]. The *Input Delay-Spread function $h(t, \tau)$* maps a transmitted signal $s(t)$ through a channel to the received signal $e(t)$ as [5, Eq. 9]:

$$e(t) = \int_{-\infty}^{\infty} h(t, t - \tau)s(\tau)d\tau.$$

Fourier transforming $h(t, \tau)$ in time gives the *Delay-Doppler-Spread function* [5, Eq. 28]:

$$U(f, \tau) = \int_{-\infty}^{\infty} e^{-j2\pi ft} h(t, \tau)dt.$$

With each channel function, Bello associates the corresponding covariance. The reason is that channel statistics and structure may be extracted from the covariance. For example, the covariance of $U(f, \tau)$ under WSSUS assumptions takes the form:

$$R_{UU}(f, \tau; f', \tau') = E[U(\tau, f)\overline{U(\tau', f')}] = P(f, \tau)\delta(f - f')\delta(\tau - \tau'),$$

where $P(f, \tau) = E[|U(f, \tau)|^2]$ is called the *scattering function*. The following examples show how the scattering function encodes the Doppler and delay distributions.

**Example 1 (PMFS)** *The* Phase-Modulation Fading Simulator *models a channel as [17]:*

$$h(t, \tau) = \frac{1}{\sqrt{N}} \sum_{n=1}^{N} a_n e^{+j2\pi f_n t} \delta(\tau - \tau_n).$$

*Then the output $e(t)$ is a sum of delayed and frequency shifted versions of the transmitted signal:*

$$e(t) = \frac{1}{\sqrt{N}} \sum_{n=1}^{N} a_n e^{+j2\pi f_n t} s(t - \tau_n).$$

*The Delay-Doppler function $U(f, \tau)$ shows this "spread" in frequency and delay:*

$$U(f, \tau) = \frac{1}{\sqrt{N}} \sum_{n=1}^{N} a_n \delta(f - f_n)\delta(\tau - \tau_n).$$

25

If the $(a_n, f_n, \tau_n)$'s are IID random variables with $a_n$'s zero mean and independent from $(f_n, \tau_n)$ then $U(f, \tau)$ is a generalized random field with covariance [1, Eq. 2.3]:

$$R_{UU}(f, \tau; f', \tau') = \sigma_a^2 p_{f,\tau}(f, \tau)\delta(f - f')\delta(\tau - \tau').$$

Thus, the scattering function registers the probability distribution $p_{f,\tau}(f, \tau)$ of the Doppler and delays. The value of the PMFS is that it provides a simple and elegant treatment of the channels functions and their covariances. However, there are non-trivial implementation and ergodic issues with the PMFS [1]. The problems may be overcome by the QMFS.

**Example 2 (QMFS)** *The* Quadrature-Modulation Fading Simulator *models a channel as North & Zeidler [29], Crohn & Bonek [12], Proakis & Salehi [35, pages 697–703]:*

$$h(t, \tau) = \sum_{n=1}^{N} a_n(t)\delta(\tau - \tau_n).$$

*The output $e(t)$ is a sum of delayed and faded versions of the transmitted signal:*

$$e(t) = \sum_{n=1}^{N} a_n(t)s(t - \tau_n).$$

Typically, the $\{a_n(t)\}$'s are complex-valued, JWSS uncorrelated Gaussian random processes with spectrum $P_{a_n a_n}(f)$ determined by the propagation environment. If the $\tau_n$'s are also independent from the $\{a_n(t)\}$'s then

$$R_{UU}(f, \tau; f', \tau') = \delta(f - f')\delta(\tau - \tau') \sum_{n=1}^{N} P_{a_n a_n}(f)p_{\tau_n}(\tau).$$

Thus, the scattering function registers the delay and fading spectrum for each path. The examples show that the interpretation of the scattering function depends on the model assumptions or the propagation environment. For this reason, an examination of the ELB propagation environment is provided in Section 3.2.

## 3.2   The Surface Scatter Model

For practical applications, such as running the LPI receiver in a channel emulator modeling ELB channels, realistic delay and Doppler distributions must be extracted from the channel measurements. This section applies Bello's *surface scatter channel* to analyze the ELB measurements. The resulting framework permits us to identify the QMFS as the channel model, set the SNR, the number of paths, their delays and amplitudes, and identify the fading processes as Ricean. Figure 3.1 illustrates the
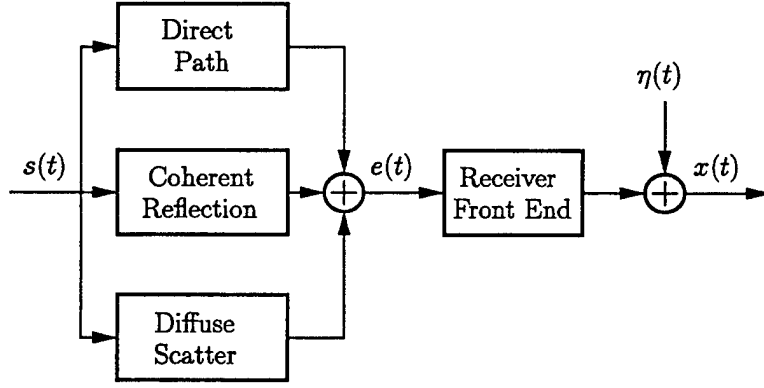
26

Figure 3.1: The surface scatter channel. From Bello [1973].

system setup. The Input Delay-Spread function $h(t, \tau)$ consists of three paths that modulate the signal $s(t)$. The signal $e(t)$ at the antenna is scaled by the receiver front end and corrupted by additive in-band RF noise and receiver noise $\{\eta(t)\}$.

Figure 3.2 illustrates the physical setup [41]. A transmitter with antenna height $h_T$ and antenna gain $G_T$ is separated by distance $d$ from the receiver with antenna height $h_R$ and antenna gain $G_R$. The direct path follows free-space propagation. The coherent reflection also follows free-space propagation but the reflection coefficient $\Gamma$ reduces power and changes phase. According to Bello [8], anything not belonging to these paths is lumped into the diffuse scatter. The Input Delay-Spread function $h(t, \tau)$ is determined as [24], [9], [26]:

$$h(t,\tau) = \sqrt{P_0} \left\{ \underbrace{L\delta(\tau - \tau_1)}_{\text{DirectPath}} + \underbrace{\Gamma\delta(\tau - \tau_2)}_{\text{CoherentReflection}} + \underbrace{g(t)\delta(\tau - \tau_3)}_{\text{DiffuseScatter}} \right\}. \tag{3.1}$$
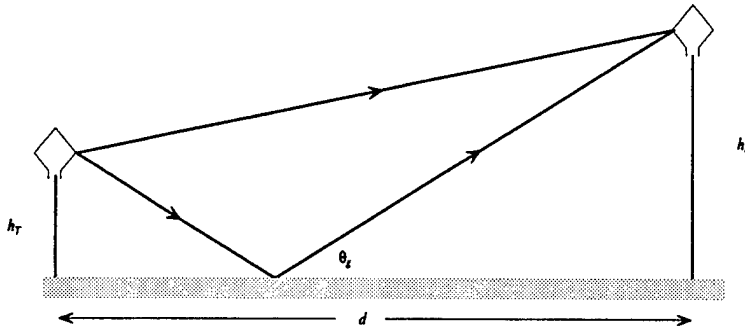


Figure 3.2: Direct path and coherent reflection. Not shown are the many paths that constitute the diffuse scatter.

27

### 3.2.1 Direct Path

Basic to propagation is the *Friis free-space transmission formula*. A transmitter with input power $P_T$ and antenna gain $G_T$ is broadcasting into free-space at wavelength $\lambda$. At a distance $r$, the receiver intercepts the radiated power with antenna gain $G_R$ equal to the directivity. The ratio of the received free-space power $P_0$ to the transmitted power $P_T$ is [11], [41, page 68], [10, page 26], [22, page 239]:

$$G_0 = \frac{P_0}{P_T} = G_T G_R \left(\frac{\lambda}{4\pi r}\right)^2. \tag{3.2}$$

Additional losses on the direct path of Equation 3.1 are modeled by $L$. The line-of-sight (LOS) simulations take $L = 1$. Loo & Secord [24] extend $L$ to a log-normal process $\{L(t)\}$ which models fast fading due to foliage. North [28] extends $L$ to include multiplicative noise on the direct and specular paths.

### 3.2.2 Coherent Reflection

A standard factorization for $\Gamma$ is [8], [32, pages 19–22], [41, pages 69–71] [23, page 95–125]:

$$\Gamma = D\Gamma_0\mathcal{R}. \tag{3.3}$$

*Divergence:* The divergence $D$ [23, page 98] "is equivalent to a purely geometric factor that describes additional spreading of a beam of rays due to reflection from a spherical surface" and has values between 0 and 1. A flat earth sets $D = 1$. We use the non-linear formula in Kerr [21, page 113].

*Plane Surface Reflection Coefficient:* $\Gamma_0$ denotes the reflection coefficient for a plane surface of the same material. For vertical polarization, [23, page 99], [10, page 53]:

$$\Gamma_0 = \frac{\epsilon\sin(\theta_g) - \sqrt{\epsilon - \cos(\theta_g)^2}}{\epsilon\sin(\theta_g) + \sqrt{\epsilon - \cos(\theta_g)^2}}, \tag{3.4}$$

where the grazing angle is

$$\theta_g = \arctan\left(\frac{h_T + h_R}{d}\right), \tag{3.5}$$

and $\epsilon$ is the complex permittivity of the terrain. Figure 3.3 plots $\Gamma_0$ for seawater and vertical polarization as a function of the grazing angle.

*Roughness Coefficient:* The roughness coefficient $\mathcal{R}$ was developed from experimental observations [4], [20], [3] and compares well with other work [23, page 122–125]. We use the modified version [10, Equation 2.62]:

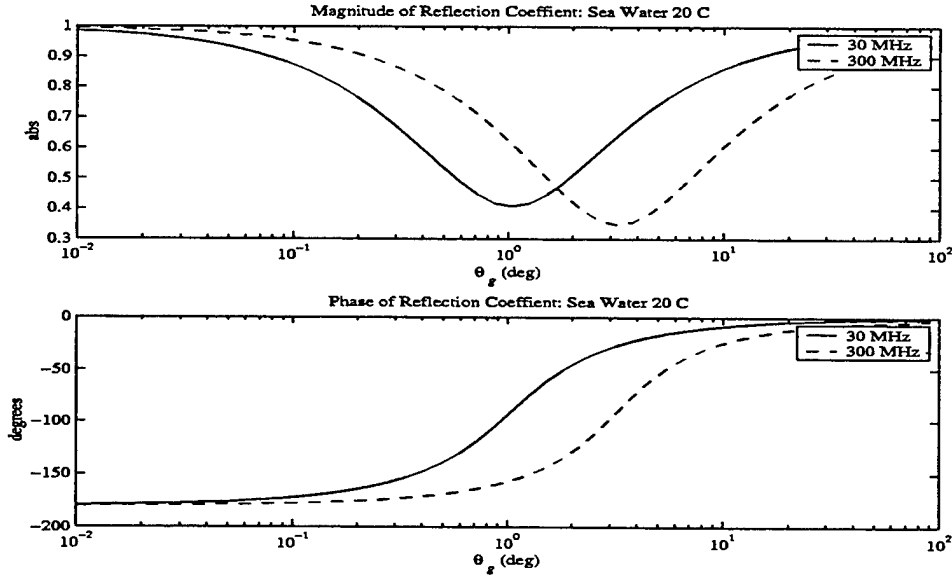$$\mathcal{R} = e^{-g^2/2}I_0(g^2/2), \tag{3.6}$$

Figure 3.3: Magnitude and phase of the reflection coefficient $\Gamma_0$ for seawater at 20° C and vertical polarization as a function of the grazing angle $\theta_g$. Here, $\epsilon = 70 - j300/\lambda$.

where **g** is the "electrical roughness parameter" [8]

$$\mathbf{g} = \frac{4\pi\Delta h \sin(\theta_g)}{\lambda}, \tag{3.7}$$

and $\Delta h$ denotes the standard deviation of the height fluctuation of the surface. [32, page 59], Long [23, page 50–54].

*Delays*: With the speed of propagation given by $c$, the direct path's time delay is

$$\tau_1 = c^{-1}\sqrt{d^2 + (h_R - h_T)^2}. \tag{3.8}$$

For each frequency, the direct and reflected signals combine at the receiver. The longer path of the reflected signal induces a phase delay $\Delta\phi$ given by [41, page 70]:

$$\Delta\phi = 2\pi f_c(\tau_2 - \tau_1). \tag{3.9}$$

### 3.2.3  Diffuse Scatter

The diffuse scatter is modeled by the zero-mean, narrowband complex-valued Gaussian random process $\{g(t)\}$. Consequently, only the spectral shape and variance needs to be specified. There is a fascinating mapping wherein the real-world propagation manifests itself in the spectral shape [15]. Table 3.1 lists selected power spectra and their associated environments.

29

Table 3.1: Fading Processes

| Fading Process | Application | References |
|---|---|---|
| Gaussian | Air-to-air, air-to-satellite | [8], [9], [16] [26] [40] |
| Bessel | Land mobile whip antenna | [41, page 150], [32, page 177] |
| Butterworth | Land mobile to satellite | [24], [25] [25] |

*Gaussian:* The fading process $\{a(t)\}$ has normalized power spectrum

$$P_{aa}(f) = \exp(-(f/(2\pi f_D)^2)$$

and a Gaussian correlation function [8], [9]. Here $f_D$ denotes the maximal Doppler frequency [41, page 128]: $f_D = v/\lambda$ with $v$ the radial speed between the transmitter and the receiver and $\lambda$ the carrier wavelength.

*Bessel:* The fading process $\{a(t)\}$ has a normalized power spectrum [32, page 117], [41, page 150]

$$P_{aa}(f) = \begin{cases} (1 - (f/f_D)^2)^{-1/2} & |f| < f_D \\ 0 & \text{elsewhere} \end{cases},$$

that gives a Bessel function for its correlation. This fading model is commonly used for land-mobile links. Parsons [32, pages 114-120] has a fine discussion showing that this spectrum is the result of assuming the multipaths are distributed around a vertical whip antenna uniformly in azimuth but with zero elevation. Allowing a small variance in elevation rolls off the poles.

*Butterworth:* The normalized power spectrum is [24]

$$P_{aa}(f) = \begin{cases} (1 + (f/f_D)^{2k})^{-1} & |f| < f_D \\ 0 & \text{elsewhere} \end{cases},$$

and is used to model both multiplicative and the log-normal noise for land-mobile satellite links in the L band.

*Power Level:* There remains the problem of setting the power level. The variance $\sigma_g^2$ is determined by the surface roughness. Beard, Katz, and Spetner [4] used the aeronautical channel model to obtain estimates of $\sigma_g$. They reported $\sigma_g/|\Gamma_0|$ was approximately constant as a function of the electrical roughness parameter and was bounded between 0.2 and 0.4. However, later measurements reported by Beard [3] showed $\sigma_g/|\Gamma_0|$ was not constant. Although Bello [8] developed approximations to this ratio, Ryan [5] argues from conservation laws that $\sigma_g = G_f|\Gamma_0|\sqrt{1 - \mathcal{R}^2}$ where $G_f$ denotes the "forward-scatter" gain.

---

[5]Frank J. Ryan [1996]: Personal communication.

## 3.2.4 Additive Noise

Figure 3.4 presents a simplified front end of the receiver. The baseband signal at the antenna $e(t)$ is scaled by the receiver's antenna gain $G_R$ and cable losses $L_{\text{cable}}$ at the receiver input. The baseband noise $\{\eta(t)\}$ arises from the RF background and system noise at the receiver input. Thus, the baseband receiver input is:
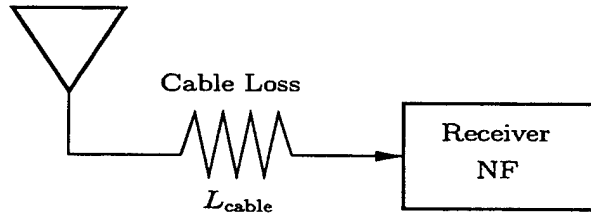
$$x(t) = G_R e(t)/L_{\text{cable}} + \eta(t).$$



Figure 3.4: Receiver front end.

The RF background noise and system noise is generally taken to be zero-mean white Gaussian noise with flat spectrum [36, 236–257], [41, page 310], [9], [40], [13], [39]. By Baseband Assumption B-2, this channel noise is linearly demodulated, shaped by the receiver's matched filter $p_R(t)$, and then presented to the detector. Thus, the baseband noise $\{\eta(t)\}$ is complex-Gaussian with flat spectrum across the passband of $p_R(t)$. Only the variance $\sigma_\eta^2$ or in-band background noise power $P_\eta = \sigma_\eta^2$ is needed to completely specify $\{\eta(t)\}$. From [22, page 76]:

$$P_\eta = \sigma_\eta^2 = kT_{\text{op}}B, \tag{3.10}$$

where $k$ is Boltzmann's constant ($1.38 \times 10^{-23}$ W K$^{-1}$ Hz$^{-1}$), $B$ is the bandwidth of $p_R(t)$ (Hz), and $T_{\text{op}}$ denotes the equivalent operating temperature (K). The literature on $T_{\text{op}}$ is extensive and the excellent review by Pritchard [33] is adapted as follows. With respect to the input to the receiver, a simplified model for a whip antenna is

$$T_{\text{op}} = \{G_R T_{\text{sky}} + T_{\text{ant}}\}/L_{\text{cable}} + T_{\text{cable}}(1 - 1/L_{\text{cable}}) + T_{\text{rcr}}.$$

The thermal noise sources are the equivalent temperatures of the antenna $T_{\text{ant}}$, the cable $T_{\text{cable}}$, and the receiver $T_{\text{rvr}}$. The receiver's antenna gain $G_R$ amplifies the RF noise from the sky $T_{\text{sky}}$. Figure 3.5 is adapted from Kim & Muehldorf [22, page 74] and gives $T_{\text{sky}}$ as a function of frequency for RF noise sources.
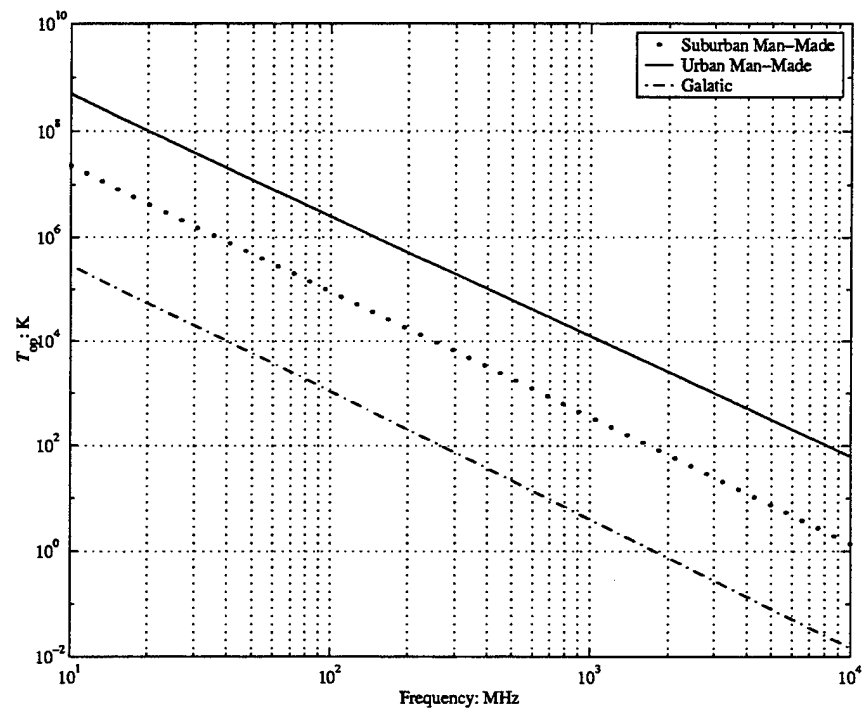
31

Figure 3.5: Sky temperatures $T_{sky}$ (Kelvins) caused by background noise sources. From Kim & Muehldorf [1995].

## 3.3 ELB Measurements

### 3.3.1 Equipment Configuration

Figure 3.6 shows the configuration of the mobile transmitter, carried on the USS *Princeton* or the HMMWV, and the fixed-site receiver. A 511 pseudorandom bit pattern was continuously transmitted from the mobile using BPSK at 231.5 MHz, 40 Watts, 999,995 bps on a raised cosine waveform. Over-the-air operation in the San Diego area requires an OA/9123 multicoupler as a pre- and post-selection filter to prevent transmit jamming of nearby receivers and to reduce adjacent channel effects when received signal strength is low. The signal was sampled using the AST195 at 12 Msps to obtain approximately 5.6 seconds of contiguous data. The SABRE GPS beacon system transmitted once a minute on UHF LOS at 270.75 MHz. The received GPS beacon information was displayed on a JMCIS terminal giving the location, bearing, velocity, and past track information.
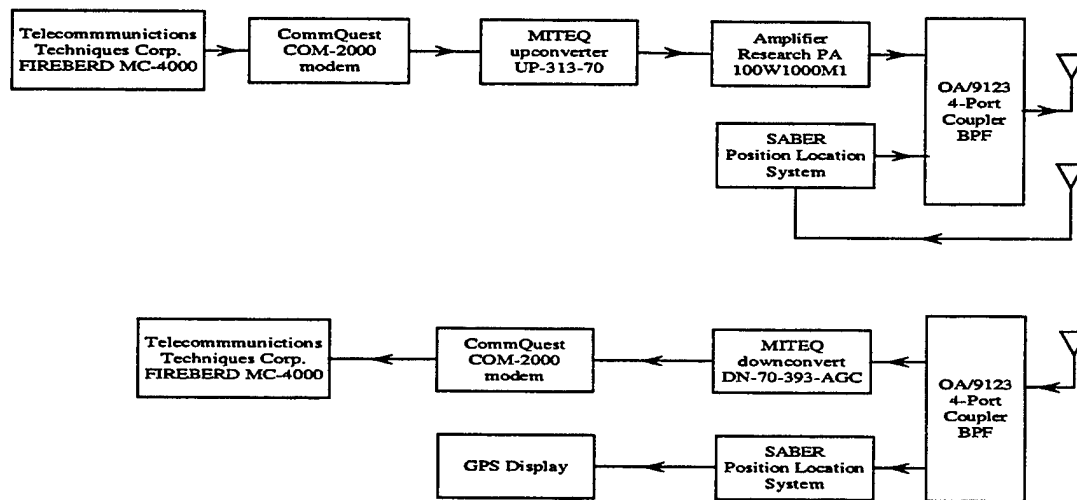
Figure 3.6: Transmit and Receive configuration.

33

## 3.3.2 Routes of the USS *Princeton*

Figures 3.7, 3.8, and 3.9 show the USS *Princeton*'s location during the experiment conducted on 21-22 January 1998. The collected channel soundings are representative of the Naval littoral environment for the Military UHF band. Ranges were extended because of a strong and persistent ducting condition that existed during these tests. A 90-nmi range was obtained by the SABRE GPS beacon during the night of 21 January 1998 (Figure 3.8). The radar range to the horizon is approximately 35 nmi.
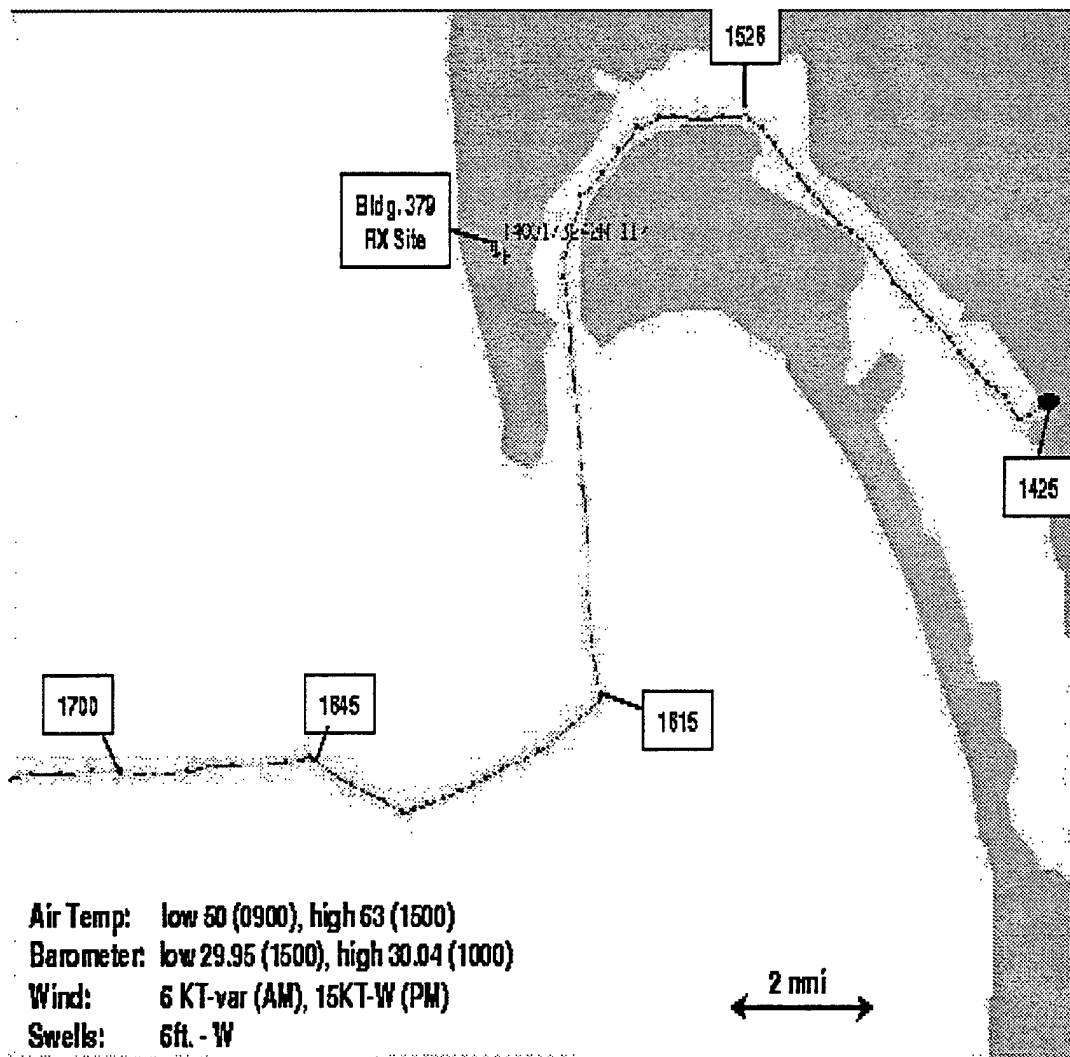


Figure 3.7: Position tracks for the USS *Princeton* on 21 January 1998 departing Port of San Diego.
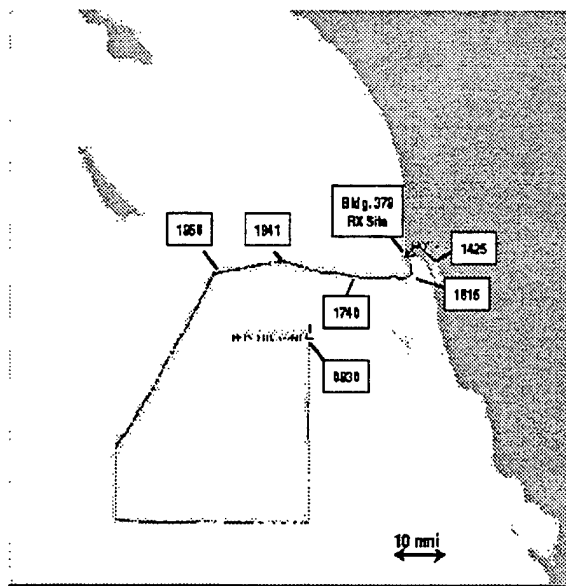
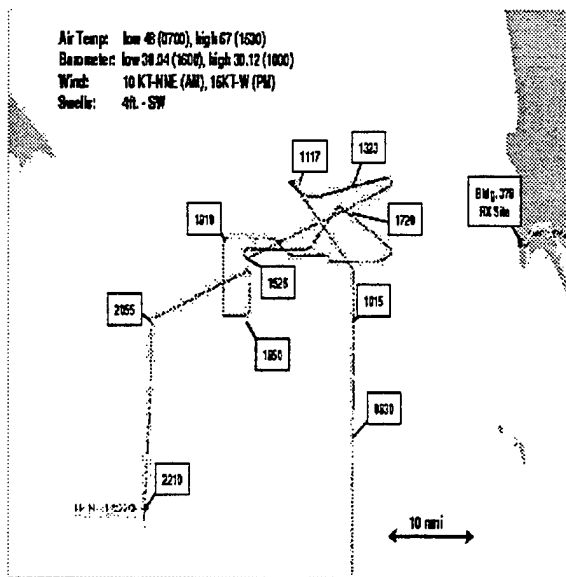Figure 3.8: Position tracks for the USS *Princeton* on 21 January 1998.



Figure 3.9: Position tracks for the USS *Princeton* on 22 January 1998.

35

### 3.3.3 HMMWV Routes

Figure 3.10 maps the HMMWV route through San Diego on 16 January 1998. From 1306 to 1320, the HMMWV traveled along Catalina Boulevard. This route traverses a residential community consisting of one-story wood houses lining both sides of the two-lane road. From 1320 to 1332, the HMMWV traveled on typical interstate freeways at approximately 55 mph, passing through downtown San Diego from 1328 to 1330. Downtown San Diego is home to 20 to 30 high-rises and numerous multi-story office buildings. From 1332 to 1340, the HMMWV navigated the relatively small streets near and on the Naval Station San Diego (NAVSTASD). NAVSTASD has numerous two- to four-story concrete buildings close to the waterfront. Navy ships line the piers on the waterfront.
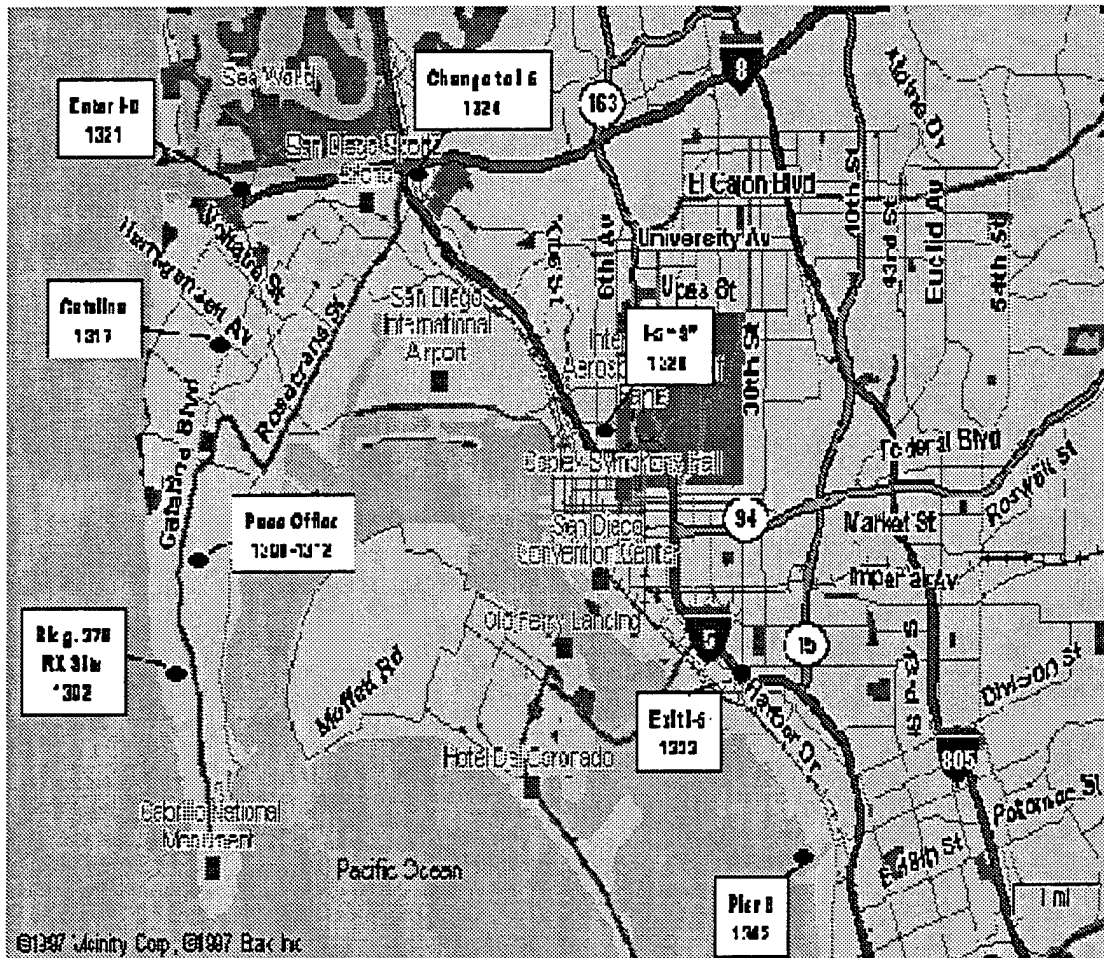


Figure 3.10: HMMWV's position track on 16 January 1998.

36

### 3.3.4 An ELB Model

We close this section by comparing the measured power levels with the power levels predicted by the model in Equation 3.1. For narrowband signals, it is standard to approximate the effect of the direct and reflected paths with a phase delay. Mathematically, the claim is [41]:

$$
\begin{aligned}
h(t,\tau) &= \sqrt{P_0}\{L\delta(\tau-\tau_1) + \Gamma\delta(\tau-\tau_2) + g(t)\delta(\tau-\tau_3)\} \\
&\approx \sqrt{P_0}\{L + \Gamma_0 D\mathcal{R}e^{-j\Delta\phi} + g(t)\}\delta(\tau-\tau_1),
\end{aligned}
\tag{3.11}
$$

where the stationarity of the $\{g(t)\}$ absorbs the delay. Thus, the surface scatter model implies Ricean fading.

How well does this model explain the measured power levels? Table 3.2 lists the relevant physical parameters for the surface scatter model. The goal is to provide an upper bound on the received power. Thus, the antenna gains are maximal and no shadowing by ship or shore is modeled. Additional assumptions are as follows: (1) The direct path takes $L = 1$; (2) The Gaussian fading is small, especially in bluewater, so $g(t) = 0$; (3) The additive noise is small. Selecting the "Urban Man-Made" from Figure 3.5 gives a sky temperature that dominates the receiver temperature. The additive noise power with respect to $P_T$ is $10\log_{10}(P_\eta/P_T) = -149$ dB. Thus, the noise level may be ignored until the USS *Princeton* nears the horizon. Figure 3.11 compares the measured data to the free-space and the surface scatter models. Point Loma shadows the transmissions until the ship rounds the point. Past this point, this model bounds most of the data but does not capture wide variations in the power levels. Some variation may be caused by shadowing of the transmitter by the maneuvering ship. Other variations could be caused by ducting. Nonetheless, that this simple model gives a good upper bound suggests the bluewater ELB channels is amiable to propagation modeling.

Table 3.2: Ship-to-Shore parameters: estimates biased high to get upper bounds on received power

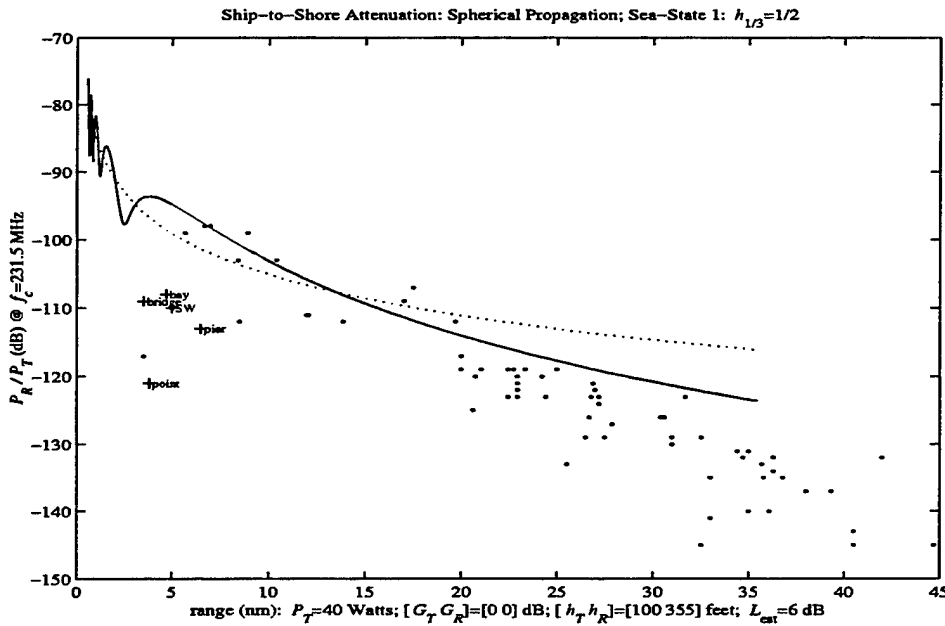| Parameter | Symbol | Value |
|---|---|---|
| Ship: antenna height | $h_T$ | 100 feet |
| gain | $G_T$ | 0 dB |
| power | $P_T$ | 40 Watts |
| Shore: antenna height | $h_R$ | 355 feet |
| gain | $G_R$ | 0 dB |
| Carrier frequency | $f_c$ | 231.5 MHz |
| Receiver Noise Figure | NF | 8 dB |
| Cable Loss | $L_{cable}$ | 6 dB |
| Cable Temperature | $T_{cable}$ | 290 K |
| Antenna Temperature | $T_{ant}$ | 100 K |
| Polarization | | vertical |
| Sea State 1 | $h_{1/3}$ | 0.5 feet |



Figure 3.11: ELB propagation measurements compared to free-space (dotted) and the surface scatter model (solid). The +'s mark measurements in San Diego Bay shadowed by Point Loma. The additive noise level is estimated as $10\log_{10}(P_\eta/P_T) \approx -149$.

## 3.4 Channel Estimation

Examples 1 and 2 show that one must have a theoretical model to interpret the scattering function. In practice, the scattering function must be estimated from a finite number of discrete samples of the noisy, distorted, received signal demodulated to baseband. Consequently, these effects could confound interpretations of the scattering function. In our setup, the digital baseband Delay-Spread function $h_B(m,k)$ is smeared in delay by the raised cosine filter $x_{RC}(t)$ as [1, Section 3.4]:

$$h_B(m,k) = x_{RC} *_\tau h(mT/O_s, kT/O_s),$$

where $O_s=12$ is the oversampling rate. The digital baseband Delay-Doppler function $U_B(f,k)$ links to $U(f,\tau)$ as [1, Section 3.5]:

$$U_B(f,k) = x_{RC} *_\tau U(f, kT/O_s)$$

and the digital baseband scattering function $P_B(f,k)$ links to the scattering function $P(f,\tau)$ as

$$P_B(f,k) = x_{RC}^2 *_\tau P(f, kT/O_s).$$

Thus, the channel functions are smeared by the raised cosine filter.

Channel estimates are also corrupted by system distortion, noise, and demodulation effects. For this reason, the NCC Dataset also contains extensive files for calibration and emulated RF channels [1, Chapters 7 & 8]. Among candidate channel estimators, an adaptive filter estimate $h_{AF}(t,\tau)$ of $h(t,\tau)$ was found to be most robust against these effects. It has a spurious-free dynamic range of -42 dB and registers the distortion of the raised cosine caused by the OA/9123 multicoupler. A DFT of $h_{AF}(t,\tau)$ gives an estimate of the Delay-Doppler function. The estimated scattering function is obtained by averaging the magnitude square of these Delay-Doppler estimates.

As a final result, QMFS channel parameters are extracted and tabulated for subsequent use in RF channel emulators. Specifically, best $N$-path channel models of the form:

$$\tilde{h}(t,\tau) = \sum_{n=1}^{N} \tilde{a}_n(t)\delta(\tau - \tilde{\tau}_n)$$

are obtained as follows. For each $t_m = mT/O_s$, the 2-norm distance between $h_{AF}(m,:)$ and $\tilde{x}_{RC} *_\tau \tilde{h}(t_m,:)$ is minimized subject to physical and RF constraints. For example, the direct and reflected paths in the bluewater ship experiments cannot be resolved in time. Thus, only one path should be present. As the sum of two passive paths, its amplitude should be not exceed 2. More importantly, the multicoupler distorts the raised cosine. Attempts to fit a raised cosine model to this distorted data produce bogus paths. To correct for this distortion, a model for the distorted raised cosine $\tilde{x}_{RC}(t)$ was obtained from the laboratory reference data [1, Chapters 7 & 8]. This distorted raised cosine $\tilde{x}_{RC}(t)$ model is used to fit the channel.

### 3.4.1  Ship-to-Shore: Bluewater

Data sets were collected from the USS *Princeton* while departing San Diego Bay on 21 January 1998 and off the coast of Point Loma on 22 January 1998. These data sets are representative of the Naval littoral environment for the Military UHF band at ranges of 3 to 40 miles. Figure 3.12 is a typical estimate of the bluewater scattering function. The trailing bands in delay arise from the raised-cosine waveform distorted by the OA/9123 multicoupler. To see this, Figure 3.13 shows the estimated PDP plotted against a reference PDP derived from the laboratory reference data. The standard two-path reflection model predicts a path delay of 0.44 ns. Combined with the sampling interval of 83 ns, the two paths have near-perfect overlap. Thus, the trailing bands arise from the distorted raised cosine waveform. With near perfect overlap, a single path model was fit to $h_{\mathrm{AF}}(t,\tau)$ with the amplitude constraint $|\tilde{a}_1(t)| \leq 2$. The estimated fade rate $\hat{f}_e \approx 0.54$ Hertz is in concordance with the maximal Doppler $f_D \approx 2.7$ Hertz. However, this amplitude estimate exhibits a slowly-varying trend that lowers the fade rate estimate and confounds PDF identification. When this trend was removed, the $\tilde{f}_e \approx 1$ Hertz and the detrended amplitude is identified as Gaussian or nominally Ricean with $K = (s/\sigma)^2 = 377$.
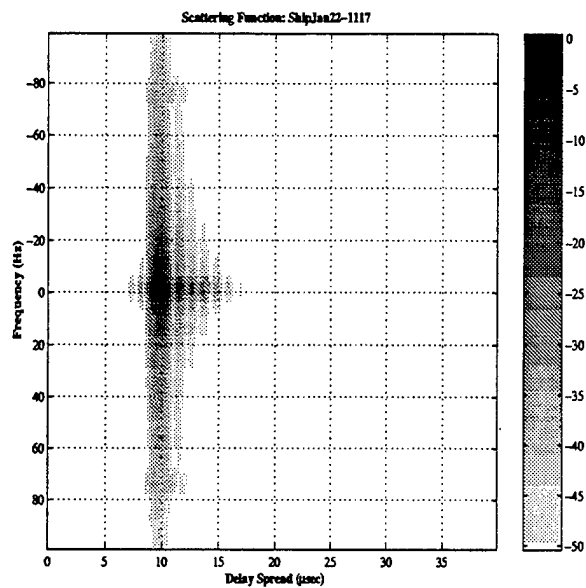
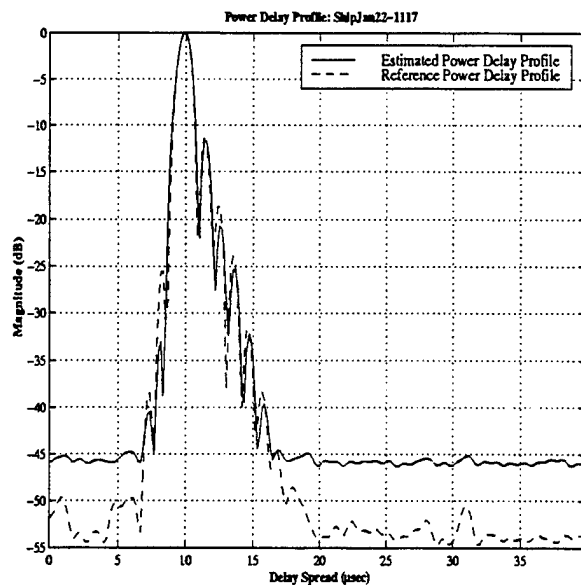Figure 3.12: Bluewater scattering estimate 26.8 nm west of Point Loma; 14 averages.



Figure 3.13: Bluewater power delay profile.

41

### 3.4.2 Ship-to-Shore: Harbor

In contrast to this bluewater data, Figure 3.14 shows the estimated scattering function for the ship in the San Diego harbor near the Coronado bridge. There is a distinct second path delayed by $\Delta\tau \approx 2\mu s$ and shifted $\Delta f \approx$-5 Hertz from the direct path. In addition, multiple paths extending to 38 $\mu s$ are present and these are also shifted by -5 Hertz. Figure 3.15 registers these delays in the estimated PDP and exhibits the strong second path. A two-path fit to $h_{\mathrm{AF}}(t,\tau)$ is also shown in Figure 3.15. These two paths are relatively uncorrelated and model most of the channel features. Table 3.3 reports the relevant path parameters as mean values referenced to Path 1 ($f_e$ excepted).

Table 3.3: Two-Path fit to Harbor; Path 1 nominally Ricean; Correlation is 0.27. The "$\Delta$" denotes the mean deviation from Path 1. Power normalized to Path 1.

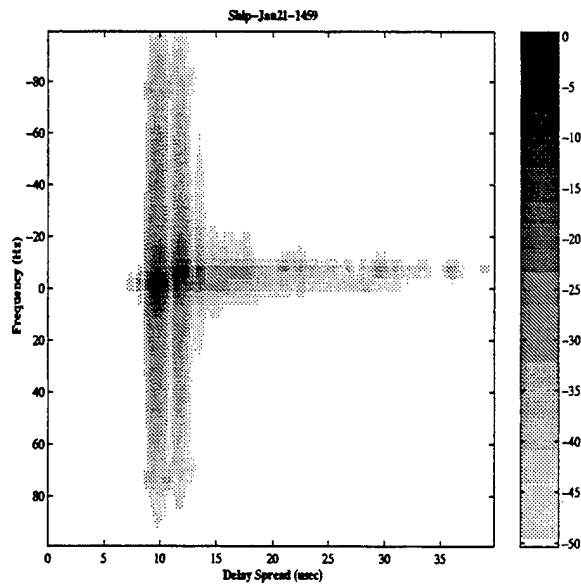| Path | Delay $\Delta\tau$ ($\mu s$) | Power dB | Doppler shift $\Delta f_D$ (Hz) | Fade rate $f_e$ (Hz) | Fading PDF |
|------|------|------|------|------|------|
| 1 | 0.0 | 0.0 | 0 | 1.6 | Ricean: $K$=136 |
| 2 | 2.0 | -4.9 | -5 | 3.8 | Ricean: $K$=14.3 |

Figure 3.14: In-harbor scattering estimate near Coronado Bridge; 14 averages.
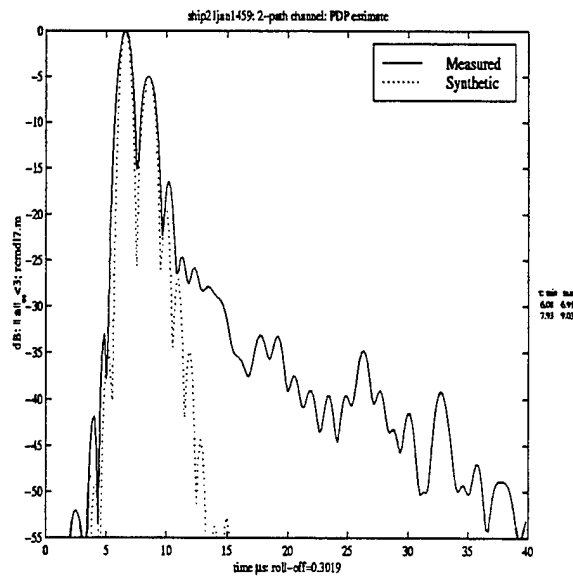


Figure 3.15: In-harbor power delay profile and two-path model.

43

## 3.4.3 HMMWV-to-Shore: Urban Freeway

Representative of the HMMWV measurements is the channel sounding collected on 16 January 1998 at 13:25 while the HMMWV was driving south on I-5 near the San Diego airport at approximately 55 mph. Figure 3.16 plots the estimated power delay profile. The main lobe is wider than that of the laboratory or ship data and registers a secondary path at 18 $\mu$s relative delay implying that this channel is dispersive with respect to the 1-MHz bandwidth. Figure 3.17 plots the estimated scattering function and shows that the secondary path is shifted by 13 Hertz. Moreover, there are several paths trailing the main path. Comparison with the power delay profile and the delay-spread function shows that these paths contribute to the extra width of the main lobe. In contrast to the simple two-path model for the ship, a multiple-path model is required to capture the features of this channel. A four-path model was fit to the data. Paths 1, 2, and 3 track the main lobe while Path 4 tracks the secondary path. Figure 3.16 shows that this model fit the channel. Table 3.4 records the results. Because Path 2 is slightly stronger than Path 1, the channel is non-minimum phase. Path 4 is relatively weaker and could be omitted from simulations. Also, the corresponding correlation matrix in Equation 3.12 demonstrates that the mainlobe paths are highly correlated.

Table 3.4: Four-Path fit to the HMMWV; Path 2 nominally Ricean. The "$\Delta$" denotes the mean deviation from Path 1. Power normalized to Path 1.

| Path | Delay $\Delta\tau$ ($\mu$s) | Power dB | Doppler shift $\Delta f_D$ (Hz) | Fade rate $f_e$ (Hz) | Fading PDF |
|------|------|------|------|------|------|
| 1 | 0.00 | 0.0 | 0 | 7 | Ricean: $K=2.6$ |
| 2 | 0.98 | +0.5 | 0 | 7 | Ricean: $K=1.1$ |
| 3 | 2.17 | -4.1 | 1 | 6 | Weibull: $K=2.0$ |
| 4 | 18.16 | -20.5 | 13 | 4 | Ricean: $K=19$ |

$$|\rho_{\mathbf{aa}}| = \begin{bmatrix} 1.00 & 0.93 & 0.71 & 0.01 \\ 0.93 & 1.00 & 0.89 & 0.02 \\ 0.71 & 0.89 & 1.00 & 0.04 \\ 0.01 & 0.02 & 0.04 & 1.00 \end{bmatrix} \qquad (3.12)$$
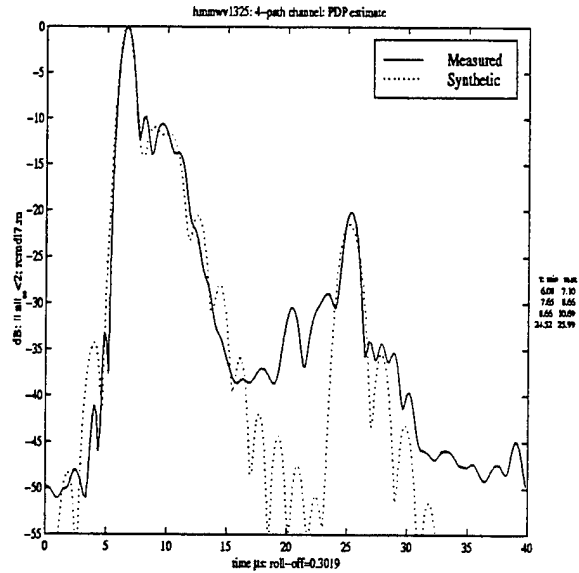
Figure 3.16: Power delay profile estimate for the HMMWV in San Diego (55 mph) and a four-path model.
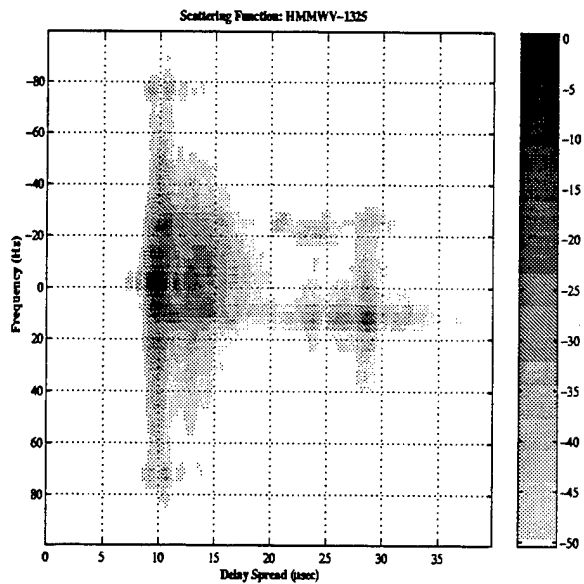


Figure 3.17: Scattering estimate for HMMWV in San Diego; 55 mph; 14 averages.

45

# 4

# LPI Performance in ELB Multipath

Section 2 obtained the LPI performance in the AWGN channel. Section 3 obtained the fading parameters for three ELB channels. This section combines these results to simulate LPI system performance the ELB channels to assess multipath effects.

Before we begin this task, we need to extend the SNR definition to handle multipath and the LPI receiver. One SNR definition considers all multipath arrivals as the signal. For the QMFS (Example 2), the received "signal" is therefore

$$e(t) = \sum_{n=1}^{N} a_n(t)s(t - \tau_n).$$

For this case, the SNR is the ratio of $\sigma_e^2/\sigma_g^2$, where $\{g(t)\}$ is the additive noise. This SNR definition is typically applied to those detectors that coherently combine the various multipaths.

Another SNR definition considers the first arrival as the signal and the other multipath arrivals as interferers. For the QMFS, the received signal is then

$$e(t) = a_1(t)s(t - \tau_1)$$

and the noise is $g(t) + \sum_{n=2}^{N} a_n(t)s(t - \tau_n)$. This SNR definition is difficult to experimentally measure because it assumes that all arriving interferers are known and can be measured. Thus, it is more appropriate for those receivers that steer nulls into the interferers.

We need an SNR definition that directly registers the multipath effects, permits immediate and unambiguous scaling to channel emulators, and also is amiable to field measurements. Typically, noise levels at the receiver are acquired by measuring the ambient power level during a lull in transmissions. With no fading, the free-space power level determines the SNR. Therefore, we elected to use this SNR in the simulations. This SNR also ties in nicely to the propagation factor for real-world measurements. For example, if there was a credible RF model for propagation, then from the measured noise levels, the RF mission planner could select a transmission power

$P_T$ to set an operational SNR. Computationally, this means that the AWGN simulations of Section 2 are replicated with the following difference. Instead of receiving $y(t) = s(t) + g(t)$, we receive

$$y(t) = \sum_{n=1}^{N} a_n(t)s(t - \tau_n) \; + \; g(t).$$

Path 1 is the first arrival with power $P_1 = E[|a_1(t)|^2]$. The SNR is set as

$$\text{SNR} = \frac{P_1}{\sigma_g^2}.$$

The relative power of the remaining paths are scaled to Path 1. No path correlations are assumed in these simulations.

This section runs the LPI-1 and LPI-2 simulations using the AWGN level of Section 2. The Bluewater, Harbor, and HMMWV multipath simulations of Section 3 are scaled by our SNR definition. Thus, any deviations from the AWGN simulations are caused by the multipath. Finally, all simulations assume a chip duration of $T_c$=10 $\mu$s.

## 4.1    LPI-1 ELB Multipath Performance

For the LPI-1 simulations, the fading processes are Ricean with Gaussian spectral shape. Referring to Section 3.2.3, this means that

$$a_n(t) = P_n \times (K_n + g_n(t)),$$

where $\{g_n(t)\}$ is a zero-mean, unit-variance, complex-valued, WSS, Gaussian random process. Its spectrum is proportional to $\exp((f/(2\pi f_D))^2)$ with $f_D$ set to the fade rate reported for the Bluewater, Harbor, and HMMWV multipath simulations. The $K_n$ is also set to the Ricean $K$ factor for these simulations. The power level is $P_n = E[|a_n(t)|^2]$ and rigged so that the relative power levels scale to the dB power levels reported for the Bluewater, Harbor, and HMMWV multipath simulations.

### 4.1.1    Performance for $[N_p, N_\Delta, N_u] = [1024, 0, 2048]$

Figures 4.1, 4.2, and 4.3 compare the performance of LPI-1 in AWGN and the multipath simulations. The LPI-1 setup is the low-dimension simulation used in Section 2.2.2. The PN sequence has length $N_u = 2048$ and is partitioned to give $L = 2$ symbol vectors of length $N_p = 1024$. With the chip duration set to $T_c$=10 $\mu$s, then the symbol vector has duration 10 ms. With all fade rates less than 5 Hertz, there is little fading variation on each symbol vector.

47

The fading is small in the Bluewater multipath. Consequently, Figure 4.1 shows little difference between the AWGN and the multipath. The Harbor multipath has two paths. The second path is delayed by $\Delta\tau = 2$ $\mu$s and 5 dB down from the first path. Figure 4.2 shows that the Harbor multipath reduced the probability of symbol error by 10 dB. In contrast, Figure 4.3 shows HMMWV multipath significantly increased the probability of symbol error. Of the four HMMWV paths, Path 1 and Path 2 both have significant fading, similar power levels, and a delay of only $\Delta\tau = 0.98$ $\mu$s. The large $K$ factors of the Ricean paths in the Harbor multipath result in a degree of temporal diversity that enhances detector performance. The smaller $K$ factors in the HMMWV multipath imply deeper fades, resulting in a symbol error floor.
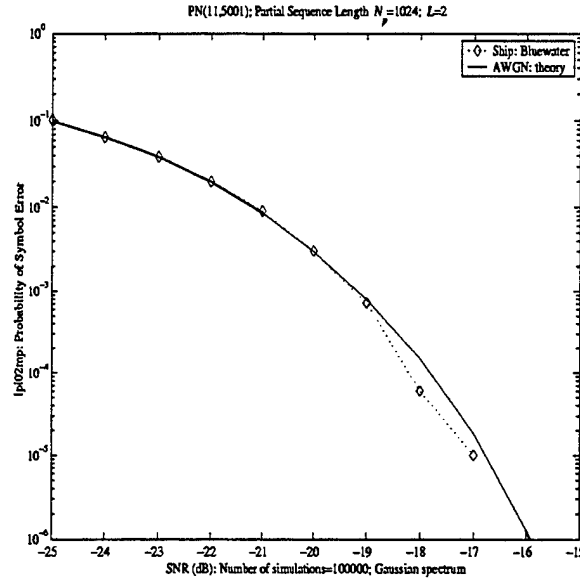


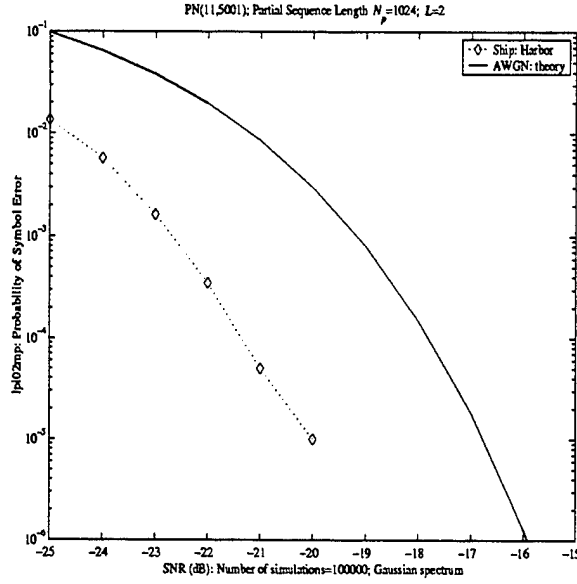Figure 4.1: LPI-1 $[N_p, N_\Delta, N_u] = [1024, 0, 2048]$ performance in Bluewater multipath.

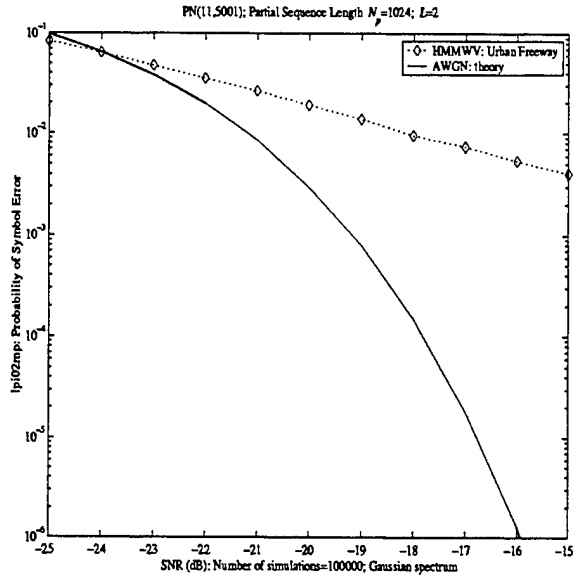Figure 4.2: LPI-1 $[N_p, N_\Delta, N_u] = [1024, 0, 2048]$ performance in Harbor multipath.



Figure 4.3: LPI-1 $[N_p, N_\Delta, N_u] = [1024, 0, 2048]$ performance in HMMWV multipath.

49

## 4.1.2 Performance for $[N_p, N_\Delta, N_u] = [1024, 0, 2^{16}]$

Figures 4.4, 4.5, and 4.6 compare the performance of LPI-1 in AWGN and the multipath simulations. This LPI-1 setup follows the setup of Section 2.2.3. The PN sequence has length $N_u = 2^{16}$ and is partitioned to give $L = 64$ symbol vectors of length $N_p = 1024$. The simulations replicate the results just obtained in Section 4.1.2: no difference between Bluewater multipath and AWGN; Harbor multipath improves performance; HMMWV multipath degrades performance. Thus, the number of symbol vectors do not affect multipath performance.
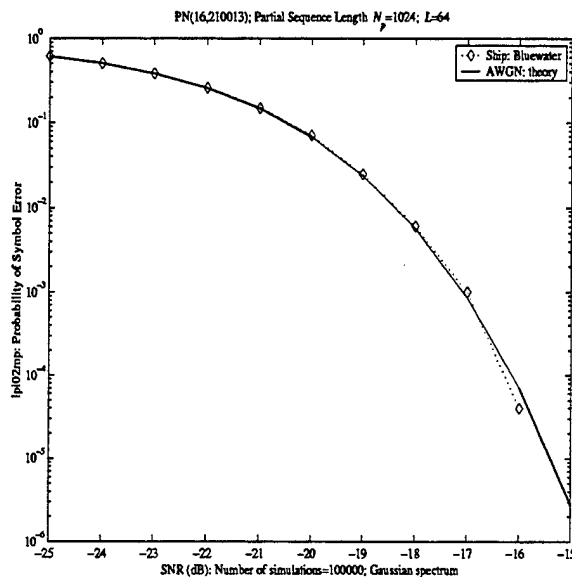


Figure 4.4: LPI-1 $[N_p, N_\Delta, N_u] = [1024, 0, 2^{16}]$ performance in Bluewater multipath.
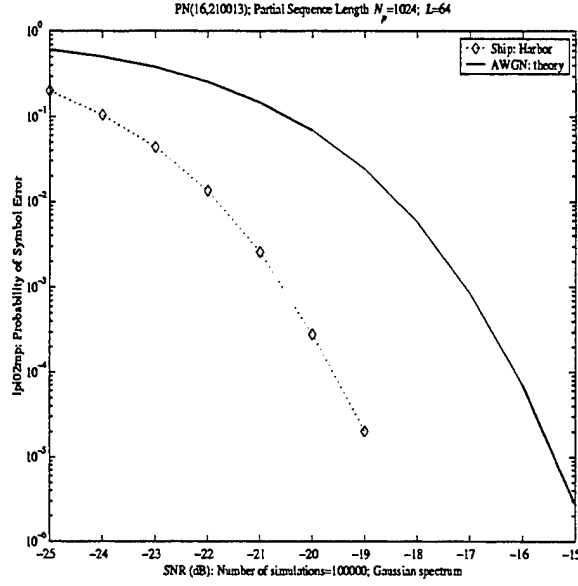
Figure 4.5: LPI-1 $[N_p, N_\Delta, N_u] = [1024, 0, 2^{16}]$ performance in Harbor multipath
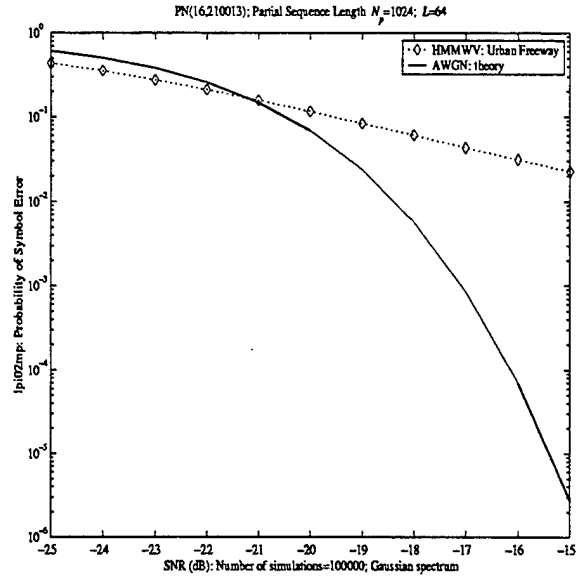


Figure 4.6: LPI-1 $[N_p, N_\Delta, N_u] = [1024, 0, 2^{16}]$ performance in HMMWV multipath

## 4.2 LPI-2 ELB Multipath Performance

Section 4.1 showed that the number of symbol vectors do not affect multipath performance. For this reason, the LPI-2 simulations were undertaken to see how the length of the symbol vectors affected multipath performance. For these LPI-2 simulations, the fading processes are Ricean with Bessel spectral shape described in Section 3.2.3. Simulations showed that for these relatively slow fade rates, changing the spectral shape between Gaussian and Bessel did not significantly affect the probability of symbol error.

The LPI-2 setup is the same as in AWGN simulations in Section 2.3. The PN sequence has length $N_u = 2^{16}$. The CCSK symbol vectors have lengths $N_p$=2048, 8192, 16384, and 65536. With the chip duration set to $T_c$=10 $\mu$s, the symbol vectors have durations 20, 82, 164, and 665 ms. Although all fade rates are less than 5 Hertz, these longer symbol vectors can have fading variations,

Figures 4.7, 4.8, 4.9, and 4.10 plot the LPI-2 performance for symbol vectors of length $N_p$=2048, 8192, 16384, 65536. Each plots shows the AWGN, Bluewater, Harbor, and HMMWV simulations. As expected, the Bluewater multipath shows little difference from the AWGN. For the Harbor multipath, LPI-2 with the short partial lengths behaves like LPI-1 with better than AWGN performance. However, as the partial length increases then LPI-2 performance degrades to AWGN performance. For HMMWV multipath, LPI-2 with short partial lengths shows worse than AWGN performance. However, increasing the partial length slowly improves LPI-2 performance. Past a threshold, there is a sudden improvement to better than AWGN performance.

So, for LPI-2 to get better than AWGN performance, we should select short partial lengths in the Harbor and a long partial length in the HMMWV. This is not immediately obvious why this is so. This contradictory performance backs the assertion in Section 1.1 that the LPI system also include an operational context. Moreover, the partial length is only one "knob" of the $[N_p, N_\Delta, N_u]$ parameters. A non-trivial question is to determine optimal LPI performance in multipath by adjusting all three parameters. Addressing this question constitutes the bulk of the Phase 4 recommendations listed in Section 1.1.
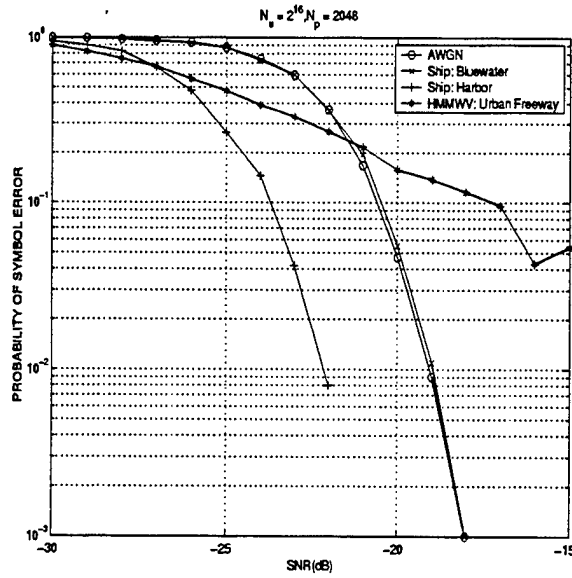
Figure 4.7: LPI-2 $[N_p, N_\Delta, N_u] = [2048, 2047, 2^{16}]$ performance in multipath
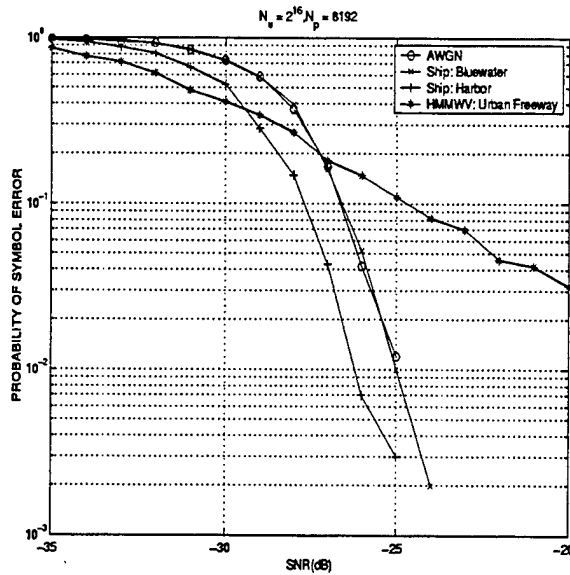


Figure 4.8: LPI-2 $[N_p, N_\Delta, N_u] = [8192, 8191, 2^{16}]$ performance in multipath.
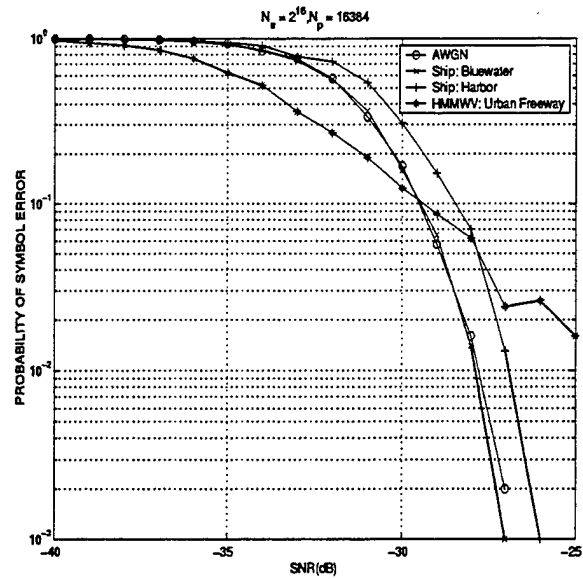
Figure 4.9: LPI-2 $[N_p, N_\Delta, N_u] = [16384, 16383, 2^{16}]$ performance in multipath.
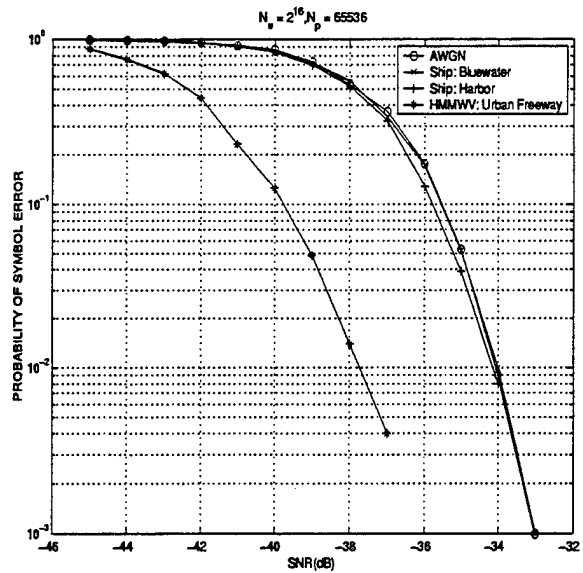


Figure 4.10: LPI-2 $[N_p, N_\Delta, N_u] = [65536, 65535, 2^{16}]$ performance in multipath.

# Bibliography

[1] Allen, J. C., M. Reuter, R. C. North [1998] *RF Channel Characterization & Estimation: Sequence-Based Methods Phase I*
http://bobcat.spawar.navy.mil/hdrlos.

[2] Allen, J. C., M. Reuter, R. C. North [1999] Scattering Functions from the Naval Communications Channel Data Base, *MilCom99.*

[3] Beard, C. I. [1961] Coherent and Incoherent Scattering of Microwaves from the Ocean, *IRE Transactions on Antennas and Propagation*, Volume AP-9, pages 470–483.

[4] Beard, C. I., I. Katz, L. M. Spetner [1956] Phenomenological Vector Model of Microwave Reflection from the Ocean, *IRE Transactions on Antennas and Propagation*, Volume AP-4, pages 162–167.

[5] Bello, Philip A. [1963] Characterization of Randomly Time-Variant Linear Channels, *IEEE Transactions on Communications Systems*, Vol. CS-11, pages 360–393.

[6] Bello, Philip A. [1965] Some Techniques for the Instantaneous Real-Time Measurement of Multipath and Doppler Spread *IEEE Transactions on Communication Technology*, Vol. COM-13, pages 285–292.

[7] Bello, Philip A. [1969] A Troposcatter Channel Model, *IEEE Transactions on Communication Technology*, Vol. COM-17, pages 130–137.

[8] Bello, Phillip A. [1973] Aeronautical Channel Characterization, IEEE Transaction on Communications, Volume COM-21, pages 548–563.

[9] Biglieri, Ezio & Valerio Zingarelli [1994] Coded Modulation for Channels Affected by Noise, Correlated Rice Fading, and Doppler Frequency Shift, *IEEE International Conference on Communications ICC '94*, New Orleans, Louisiana, USA, pages 18–22.

[10] Boithias, Lucien [1987] *Radio Wave Propagation*, McGraw-Hill Book Company, New York.

[11] Bullington, Kenneth [1956] Radio Propagation Fundamentals, *Bell System Technical Journal*, Volume 36.

[12] Crohn, Ilan & Ernst Bonek [1992] Modeling of Intersymbol-Interference in a Rayleigh Fast Fading Channel with Typical Delay Power Profiles, *IEEE Transactions on Vehicular Technology*, Volume 41, Number 4, pages 438–446.

[13] D'Andrea, A. N., A. Diglio, U. Mengali [1994] Symbol-Aided Channel Estimation With Nonselective Rayleigh Fading Channels, *IEEE International Conference on Communications ICC '94*, Volume 1, pages 316–320.

[14] Desrosiers, A. & J. Zeidler [1998] Exploration of Commercial Communications Systems for Littoral Warfare Applications, Terrestrial Link Implementation Branch, Code D846, SSC-SD.

[15] Gans, Michael J. [1972] A Power-Spectral Theory of Propagation in the Mobile-Radio Environment, *IEEE Transactions on Vehicular Technology*, Volume VT-21, Number 1, pages 27–38.

[16] Harris, R. M. [1990] Doppler-Multipath Tolerant Voice Communication *AGARD Conference Proceedings 486*, NATO, pages 31-1 to 34-10.

[17] Hoeher, Peter [1992] A Statistical Discrete-Time Model for the WSSUS Multipath Channel, *IEEE Transactions on Vehicular Technology*, Vol 41, Number 4, pages 461–468.

[18] Honig, Michael & Melbourne Barton [1996] Baseband Signaling and Pulse Shaping, in *The Mobile Communications Handbook*, Jerry D. Gibson (editor), CRC Press.

[19] Johnson, G. B. [1999] *COTS LPI Communication System Report for Fiscal Year 1998*, SPAWAR TR 1788.

[20] Katz, Isadore [1963] Radar Reflectivity of the Ocean for Circular Polarization, *IRE Transactions on Antennas and Propagation*, Volume AP-11, pages 451–453.

[21] Kerr, Donald E. [1951] *Propagation of Short Radio Waves*, McGraw-Hill, New York.

[22] Kim, John C. & Eugen I. Muehldorf [1995] *Naval Shipboard Communication Systems*, Prentice Hall PTR, Englewood, Cliffs, New Jersey.

[23] Long, Maurice W. [1983] *Radar Reflectivity of Land and Sea*, Second Edition, Artech House, Inc.

[24] Loo, Chun & Norman Secord [1991] Computer Models for Fading Channels with Applications to Digital Transmission, *IEEE Transactions on Vehicular Technology*, Volume 40, Number 4, pages 700–707.

[25] Lutz, Erich & Ernst Plöchinger [1985] Generating Rice Processes with Given Spectral Properties, *IEEE Transactions on Vehicular Technology*, Volume VT-34, Number 4, pages 178–181.

[26] Miyagaki, Yoshiya, Norihiko Morinaga, Toshihiko Namekawa [1983] Double Symbol Error Rates of $M$-ary DPSK in a Satellite-Aircraft Multipath Channel, *IEEE Transactions on Communications*, Volume COM-31, Number 12, pages 1285–1289.

[27] Miller, Kenneth S. [1974] *Complex Stochastic Processes*, Addison-Wesley, Massachusetts.

[28] North, Richard C. [1996] *Broad Agency Announcement: High-Data-Rate, Line-of-Sight Digital Radio of Mobile Maritime Communications*, N66001-96-X6911, http://www.nosc.mil/contract/baa/x6911

[29] North, Richard C. & James R. Zeidler [1994] Multichannel Adaptive Equalization for Improved Performance in LOS Digital Radio, *1994 IEEE Military Communications Conference*, Fort Monmouth, NJ.

[30] North, R. C., R. A. Axford, J. R. Zeidler [1993] The Performance of Adaptive Equalization for Digital Communication Systems, *Twenty-Seventh Asilomar Conference on Signals, Systems, & Computers*, pages 1548–1553.

[31] North, Richard C., Roy A. Axford, D. Bryan [1995] *Communications Toolbox Developed at NRaD*, Version 1.0, pre-print.

[32] Parsons, David [1992] *The Mobile Radio Propagation Channel*, Halstead Press, New York.

[33] Pritchard, Wilbur [1997] The Calculation of System Temperature for a Microwave Receiver, in *The Communications Handbook*, Jerry D. Gibson (editor), CRC Press.

[34] Proakis, John G. [1996] *Digital Communications*, Third Edition, McGraw-Hill, New York.

[35] Proakis, John G. & Masoud Salehi [1994] *Communication Systems Engineering*, Prentice Hall, New Jersey.

[36] Sakrion, D. J. [1968] *Communication Theory: Transmission of Waveforms and Digital Information*, John Wiley & Sons, Inc., New York.

[37] Sklar B. [1988] *Digital Communications*, Prentice-Hall, Englewood Cliffs, NJ.

[38] Staley, Thomas L. [1997] *Channel Estimate-Based Performance Prediction for Coherent Linearly Modulated Wireless Communication Systems*, Ph.D. Thesis, UCSD.

[39] Tan, Zhenhui & I. F. Blake [1992] Multipath Diversity Reception of Hybrid DS-SFH Spread Spectrum Multiple Access Over Rician Multipath Fading Channels, *IEEE International Conference on Selected Topics in Wireless Communications*, Vancouver, B.C., Canada, pages 433–436.

[40] Vietta, Giorgio M. & Desmond P. Taylor [1994] Maximum Likelihood Sequence Estimation of Uncoded and Coded PSK Signals Transmitted over Rayleigh Flat-Fading Channels, *IEEE International Conference on Communications ICC '94*, Volume 1, pages 1–7.

[41] Yacoub, Michel Daoud [1993] *Foundations of Mobile Radio Engineering*, CRC Press, Boca Raton.

# REPORT DOCUMENTATION PAGE

Form Approved
OMB No. 0704-01-0188

| 1. REPORT DATE *(DD-MM-YYYY)* | 2. REPORT TYPE | 3. DATES COVERED *(From - To)* |
|---|---|---|
| 09–2000 | Technical | |

**4. TITLE AND SUBTITLE**
THE EXTENDED COTS LPI COMMUNICATIONS SYSTEM
Phase 3 Performance Analysis

**5a. CONTRACT NUMBER**

**5b. GRANT NUMBER**

**5c. PROGRAM ELEMENT NUMBER**
0601152N

**6. AUTHORS**
J. C. Allen, M. Reuter, G. M. Dillard, G. Johnson, J. Zeidler

**5d. PROJECT NUMBER**

**5e. TASK NUMBER**
DN309351

**5f. WORK UNIT NUMBER**
ZU92

**7. PERFORMING ORGANIZATION NAME(S) AND ADDRESS(ES)**
SSC San Diego
San Diego, CA 92152–5001

**8. PERFORMING ORGANIZATION REPORT NUMBER**
TR 1828

**9. SPONSORING/MONITORING AGENCY NAME(S) AND ADDRESS(ES)**
Office of Naval Research
800 North Quincy Street
Arlington, VA 22217–5660

**10. SPONSOR/MONITOR'S ACRONYM(S)**

**11. SPONSOR/MONITOR'S REPORT NUMBER(S)**

**12. DISTRIBUTION/AVAILABILITY STATEMENT**
Approved for public release; distribution is unlimited.

**13. SUPPLEMENTARY NOTES**

**14. ABSTRACT**
Phase 3 of the COTS LPI effort examines two LPI systems: LPI-1 approximates an incoherent M-ary orthogonal system: LPI-2 is a variant of the cyclic code-shift keying waveform. Each LPI system is assessed using the performance vector $[P_e E_b / N_0 R / W \ SNR]^T$. The SNR is included with the three standard COMM variables as a measure of "covertness." Slices of this function are used to rank LPI-1 and LPI-2. For additive white Gaussian noise, the fundamental trade-off that emerges for fixed bandwidth W is between the SNR and the bit rate R. A more covert system requires longer symbol vectors. These longer symbol vectors lower the bit rate. The LPI performance surface permits system engineers to graphically assess the trade-offs. For the multipaths of the Extended Littoral Battlefield, simulations show that multipath may either have no effect, improve performance, or degrade performance. The basic observation is the longer symbol vectors can mitigate the multipath effects. Analysis of this multipath effect, increasing the bit rate, and migrating these results in the LPI performance surface, are the basic Phase 4 recommendations.

**15. SUBJECT TERMS**
Mission Area: Command, Control, and Communications
signal processing                undersea surveillance                image processing
array processing                electronic devices

| 16. SECURITY CLASSIFICATION OF: | | | 17. LIMITATION OF ABSTRACT | 18. NUMBER OF PAGES | 19a. NAME OF RESPONSIBLE PERSON |
|---|---|---|---|---|---|
| a. REPORT | b. ABSTRACT | c. THIS PAGE | | | J. C. Allen |
| U | U | U | UU | 72 | 19B. TELEPHONE NUMBER *(Include area code)*<br>(619) 553–6566 |

Standard Form 298 (Rev. 8/98)
Prescribed by ANSI Std. Z39.18

# INITIAL DISTRIBUTION

| | | |
|---|---|---|
| D0012 | Patent Counsel | (1) |
| D0271 | Archive/Stock | (6) |
| D0274 | Library | (2) |
| D027 | M. E. Cathcart | (1) |
| D0271 | D. Richter | (1) |
| D363 | J. C. Allen | (15) |

Defense Technical Information Center
Fort Belvoir, VA 22060–6218           (4)

SSC San Diego Liaison Office
Arlington, VA 22202–4804

Center for Naval Analyses
Alexandria, VA 22302–0268

Office of Naval Research
Attn: NARDIC (Code 362)
Arlington, VA 22217–5660

Government–Industry Data Exchange
   Program Operations Center
Corona, CA 91718–8000